Chronic demyelination of rabbit lesions is attributable to failed oligodendrocyte progenitor cell repopulation.

James J. M. Cooper, BS[1], Jessie J. Polanco, PhD[2], Darpan Saraswat, PhD[1], Jennifer Peirick, DVM[3], Anna Seidl[1], Yi Li[1], Dan Ma, PhD[4], Fraser J. Sim, PhD[1,2]

Department of Pharmacology and Toxicology[1], Neuroscience Program[2], Lab Animal Facilities[3], Jacobs School of Medicine and Biomedical Sciences, University at Buffalo, Buffalo, NY.

Translational Medicine Research Group[4], Aston Medical School, Aston University, Birmingham, United Kingdom.

Address correspondence to:

Fraser Sim, Ph.D.
Department of Pharmacology and Toxicology
Jacobs School of Medicine and Biomedical Sciences
University at Buffalo
955 Main Street
Buffalo, NY 14203
716-829-2151
fjsim@buffalo.edu

Topics: Oligodendrocyte, CNS myelin, Multiple sclerosis
Keywords: Remyelination, models

Main Points:
- Chronic demyelination in the rabbit CNS was associated with reduced OPC repopulation.
- Quiescent OPCs accumulated around the edge of rabbit lesions.
- OPC and oligodendrocyte repopulation was reduced in rabbit regardless of lesion volume.

Running title: Poor OPC Repopulation in Rabbit Demyelination
Abstract, 245; Introduction, 846; Discussion, 1787; Tables: 0, Figures: 9

Acknowledgements: This work was supported by the Department of Defense Congressionally Directed Medical Research Programs (W81XWH-21-1-0387), NINDS grant (R01NS104021), National Multiple Sclerosis Society (RG-1701-26750 and PP-1706-28080), the Kalec Multiple Sclerosis Foundation, and the Change MS Foundation. JJP received additional support from NIGMS (R25GM09545902), NCATS (UL1TR001412-S1), and New York State Department of Health (Empire State Stem Cell Fund) through the Stem Cells in Regenerative Medicine Fellowship (NYSTEM C30290GG). We acknowledge support provided by the Center for Computational Research at the University at Buffalo for use of the academic compute cluster for training the Keras-based convolution network. We also thank JA17 for is his support and motivation during this project.

Conflict of Interest: The authors declare no competing financial interests.

Abstract

The failure of remyelination in the human CNS contributes to axonal injury and disease progression in multiple sclerosis (MS). In contrast to regions of chronic demyelination in the human brain, remyelination in murine models is preceded by abundant oligodendrocyte progenitor cell (OPC) repopulation, such that OPC density within regions of demyelination far exceeds that of normal white matter. As such, we hypothesized that efficient OPC repopulation was a prerequisite of successful remyelination, and that increased lesion volume may contribute to the failure of OPC repopulation in human brain. In this study, we characterized the pattern of OPC activation and proliferation following induction of lysolecithin-induced chronic demyelination in adult rabbits. The density of OPCs never exceeded that of normal white matter and oligodendrocyte density did not recover even at 6 months post-injection. Rabbit OPC recruitment in large lesions was further characterized by chronic Sox2 expression in OPCs located in the lesion core and upregulation of quiescence-associated Prrx1 mRNA at the lesion border. Surprisingly, when small rabbit lesions of equivalent size to mouse were induced, they too exhibited reduced OPC repopulation. However, small lesions were distinct from large lesions as they displayed an almost complete lack of OPC proliferation following demyelination. These differences in the response to demyelination suggest that both volume dependent and species-specific mechanisms are critical in the regulation of OPC proliferation and lesion repopulation and suggest that alternate models will be necessary to fully understand the mechanisms that contribute to failed remyelination in MS.

INTRODUCTION

Disease-modifying therapies for the treatment of relapsing-remitting multiple sclerosis (MS) are effective at limiting neuroinflammation and reduce the rate of clinical relapses (McGinley et al., 2021). However, treatment options for progressive disability in MS and agents capable of enhancing myelin repair are limited. The stimulation of remyelination has been proposed to restore neurological function and prevent neurodegeneration in regions of chronic demyelination. Although spared oligodendrocytes (OLs) may contribute to remyelination in MS and in some experimental models (Yeung et al., 2019, Duncan et al., 2018, Bacmeister et al., 2020), when large numbers of adult OLs are destroyed remyelination relies on the generation of new OLs by oligodendrocyte progenitor cells (OPCs) (Hughes et al., 2013, Zawadzka et al., 2010). The cellular processes of remyelination can be broadly divided into recruitment and differentiation phases (Franklin and Ffrench-Constant, 2017). During the recruitment phase, OPCs upregulate markers of activation, enter the cell-cycle and migrate into the demyelinated lesion resulting in tissue repopulation. The expression of activation markers, such as Sox2, are then downregulated as OPCs differentiate into OLs (Zhao et al., 2015). The differentiation phase occurs when OPC exit the cell cycle and differentiate into myelin-forming oligodendrocytes (Franklin and Ffrench-Constant, 2017). Newly generated OLs engage and ensheath denuded axons and upregulate myelin proteins resulting in the production of a thin myelin sheath with shorter internodes that is capable of restoring saltatory conduction (Lubetzki et al., 2020).

While remyelination is a common feature of early relapsing-remitting MS, remyelination failure becomes more common with increasing disease duration and age (Franklin and Ffrench-Constant, 2017, Neumann et al., 2019). Remyelination failure is thought to be due to the malfunction of one or more stages of OL regeneration: namely OPC recruitment, differentiation, or myelin formation (Franklin and Ffrench-Constant, 2017). While quiescent OPCs are associated with chronic demyelination in MS (Wolswijk, 1998), the prevailing theory in the field has been that remyelination fails in MS due to a failure of differentiation. In response, a number of drug candidates aimed at boosting endogenous remyelination through the promotion of OPC differentiation have been developed and advanced to clinical trials after successful preclinical results, notably opicinumab (anti-Lingo1) (Mi et al., 2005), clemastine (Mei et al., 2014), and bexarotene (Huang et al., 2011). Unfortunately, while all were able to improve a functional test indicative of remyelination in the optic nerve, they have largely failed to significantly improve clinical outcomes or primary imaging endpoints in initial trials (Green et al., 2017, Mellion et al., 2017, Cadavid et al., 2019, Brown et al., 2021). The paradoxical success of differentiation-

promoting therapies in rodent models, but little success in clinical trials, suggests fundamental differences in the rate-limiting steps between remyelination in animal models and human MS.

A defining feature of human MS lesions is the dramatic increase in volume relative to murine models. Although highly variable in size, the median volume of an individual human MS lesions is around 100 mm^3 (Kohler et al., 2019), whereas typical mouse lesions are < 1 mm^3 (Jean et al., 2003, Rusielewicz et al., 2014). If the number of OLs required for successful remyelination scales linearly with lesion volume, this predicts a requirement for 100-fold more myelinating cells in MS. In the case of focal demyelination, OPCs are recruited from the surrounding white matter (Sim et al., 2002). As such, the available pool of progenitors will scale with lesion surface area which, assuming a roughly spherical lesion, increases at the square root of volume. Thus, to achieve a similar density of OPCs, a ten-fold increase in OPC generation (representing 3 or more cell divisions) and/or substantially improved migration must occur. In murine models of demyelination, the density of OPCs rapidly rises 2-3 fold above that of normal white matter shortly following lesion formation (Sim et al., 2002, Ulrich et al., 2008, Kucharova and Stallcup, 2015, Lin et al., 2006). In contrast, OPC density in MS lesions rarely exceed that of normal appearing white matter (NAWM) (Lucchinetti et al., 1999, Kuhlmann et al., 2008, Boyd et al., 2013, Moll et al., 2013, Tepavcevic et al., 2014). These observations are consistent with an inability to scale OPC recruitment as lesion size increases.

In this study, we sought to model larger volumes of demyelination which were characterized by chronic demyelination. We selected the rabbit lysolecithin model of demyelination as it was originally characterized as exhibiting chronic demyelination for at least 6 months (Blakemore, 1978, Waxman et al., 1979, Foster et al., 1980). We found that the density of OPCs never exceeded that observed in rabbit NAWM. OPC repopulation was associated with a protracted period of OPC activation and relatively poor OPC proliferation. In addition, we observed an upregulation of quiescence associated marker Prrx1 (Wang et al., 2018, Saraswat et al., 2021b) in OPCs found at the lesion border at earlier timepoints. We found that these alterations were not solely due to volume, as 10-fold smaller lesions also displayed reduced OPC density and reduced proliferation. However, small lesions were distinct in that they contained almost no proliferating OPCs. Together, these observations suggest that both volume-dependent and species-specific differences in the OPC response to demyelination contribute to the capacity of animal models to undergo spontaneous remyelination.

131 **MATERIALS AND METHODS**

132 *Animals and surgery*

133 All experiments were performed according to protocols approved by the University at Buffalo's
134 Institutional Animal Care and Use Committee. New Zealand White Rabbits were purchased as
135 needed (Female, average weight 2.96 ± 0.13 kg, and average age 15.79 ± 0.53 weeks) (Charles
136 Rivers Laboratories, Wilmington, MA). Induction anesthesia was accomplished via intramuscular
137 injection of ketamine (35 mg/kg) and xylazine (5 mg/kg) into epaxial muscles. After loss of
138 consciousness, supplemental heating began, and corneas were lubricated. The proximal 3 cm of
139 the tail was shaved to provide an optimal location for the pulse oximetry probe (far preferable to
140 use of ear or tongue). ECG leads and rectal temperature probe were placed. After pre-
141 oxygenation via face mask, rabbits were intubated in ventral recumbency with heads and necks
142 held in extension. A size 3.0 endotracheal tube was threaded over an 8-French urinary catheter.
143 After placement of the catheter through the glottis, the ET tube was advanced over the catheter
144 and into the trachea. Successful intubation was verified via immediate capnography. Upon
145 success, isoflurane was delivered via Bain Circuit (1-3%). An IV catheter was placed (marginal
146 ear vein), and the surgical site was shaved and prepped prior to moving the rabbit to the operating
147 room (OR). Pre-emptive, initial analgesics were administered (0.05 mg/kg buprenorphine,
148 subcutaneously (SC) and 1.5 mg/kg carprofen, SC).

149 Once moved onto the OR table, rabbits were immediately reconnected to isoflurane to
150 ensure a suitable anesthetic plane. Then, they were transiently disconnected from the Bain Circuit
151 to allow loose movement of the head into the stereotaxic frame (Kopf Model 902 Small Animal
152 Stereotaxic Instrument + Kopf Model 1240 Rabbit Adaptor + Rabbit Risers, Kopf Instruments,
153 Tujunga, CA). The endotracheal (ET) tube, was carefully moved to rest between the arms of the
154 Kopf Rabbit Adaptor. It was important that the ET tube was not advanced beyond 12 cm to avoid
155 bronchial obstruction. Once positioned, the capnograph and Bain Circuit were quickly
156 reconnected. At this time further careful positioning of the rabbit's head was possible via tooth
157 bar, zygoma clamps, nose clamp. General anesthesia could be maintained for the remainder of
158 the stereotaxic procedure with isoflurane. Spontaneous respirations were augmented by manual
159 intermittent positive pressure ventilations (IPPV). 0.1 mL bupivacaine (0.25%) or lidocaine (2%,
160 diluted 1:1 with 0.9% NaCl) was injected SC. A 7-8 cm incision was made alone the midline of
161 the scalp to expose both bregma (intersection of the sagittal and coronal sutures) and lambda
162 (intersection of the sagittal and lambdoid sutures). Both left and right arm Hamilton needles were
163 filled with distilled H_2O to prevent occlusion and ensure flow prior to lysolecithin loading. Placing
164 the needles point on either bregma or lambda, the dorsal-ventral (DV) relationship was adjusted

using the Kopf Rabbit Adaptor until bregma was 1.5 mm above lambda. The Rabbit Alignment Tool (Kopf Model 1244 Rabbit Alignment Tool) greatly aided the speed of this process, as well as ensuring minimal rotation about the principal axes (roll, pitch, yaw). The arms of the Kopf frame were adjusted to a 20° angle, and the needle points were placed on bregma. The anterior-posterior (AP), lateral-medial (LM), and DV of each arm was recorded. The following adjustments were made to these values: AP= +0.5 mm, LM= +7.7 mm, DV= -5.7 mm. Injection sites were confirmed previously via Evans Blue injection. Drill bits (Burrs for Micro Drill 19007-29, 2.9 mm, Foster City, CA) were sterilized via dry micro bead bench side sterilizer for 1 minute and cooled with room temp saline. In advance of drilling, topical articaine (4%) was dripped onto the skull and allowed to absorb and dry over drilling skull sites. Drill holes were made through the skull to the level of the meninges with constant saline stream to prevent parenchymal heat damage. A 30G needle was then used to puncture the meninges to allow for free passage of the Hamilton needle. 1% lysolecithin was then injected at a rate 0.1 µl/min, with 5-minute wait times between microliters to allow for diffusion. Once injection was completed, the needles were left in place for 20 additional minutes to allow for diffusion. Either 5 µL (large volume lesion) or 0.35 µL (small volume lesion) or lysolecithin was injected.

Post-operatively, buprenorphine was administered (0.05 mg/kg, SC) 4 hours after the initial dose, and carprofen (1.5 mg/kg, SC) was continued twice daily for a total of 4 consecutive days. Rabbits were monitored daily after surgery and assessed for: mentation, weight loss from baseline, appetite, water consumption, amount and character of feces, amount of urination, and presence of neurologic signs. Post-surgical weight loss peaked at 28 dpl, followed by a rapid recovery (data available upon request).

Tissue processing

Animals were sacrificed at 7, 14, 21, 56, or 180 days post-lesion (dpl) by transcardial perfusion of saline followed by 4% paraformaldehyde under deep anesthesia. Following decapitation, whole brain tissue was extracted and post-fixed for 30 minutes in 4% paraformaldehyde. For cryopreservation, the tissue was first left in 1x PBS overnight, then transferred into a 7.5% sucrose solution overnight, and finally 15% sucrose overnight. Cryoprotected tissue was then frozen in optimal cutting temperature medium (Tissue-Tek). Serial, 16 µm-thick coronal sections were cut using a Leica cryostat and stored in -80 °C freezer until processing.

To identify lesion location and volume, every 10th section was washed with 1x PBST (x3 by 5 min), stained with FluoroMyelin for 1 hour at room temperature (1:300, Thermo Fisher Scientific) and 4′,6-Diamidino-2-phenylindole dihydrochloride (DAPI) for 3 min (1:5000, Sigma

Aldrich), and mounted in prolong gold (Thermo Fisher Scientific). Lesions were identified as regions with lesser FluoroMyelin signal and corresponding hypercellularity by DAPI, compared to surrounding white matter. Cross-sectional lesion areas were calculated for both left and right hemisphere lesions using the NIH ImageJ software, and the largest cross-sectional area for each lesion was identified as the lesion center.

Estimation of lesion volume

Lesion volume was calculated from the measured cross-sectional areas determined by FluoroMyelin staining using Cavalieri's estimator of morphometric volume (Rosen and Harry, 1990):

$$V_c = d\left(\sum_{i=0}^{n}(y_i)\right) - (t)y_{MAX}$$

Where V_c is the Cavalieri's estimated volume, d is the distance between sections, y_i is the cross-sectional area of section i, t is the thickness of the sections, and y_{MAX} is the largest cross-sectional area of the lesion. Since every 10th section was stained, d = 160 μm, and t = 16 μm.

Immunohistochemistry (IHC)

Slides immediately adjacent to the lesion centers, identified by FluoroMyelin staining, were used for all immunohistochemical procedures. In general, sections were permeabilized for 1 hour with 1% Triton X-100 (Alfa Aesar) and 0.25% Tween 20 (Calbiochem). Sections were blocked for 1 hour with a solution containing 0.5% Triton X-100, 5% bovine serum albumin (BSA), and 5% normal donkey serum. For cytoplasmic antigens such as CC1, sections were permeabilized with a 0.1% saponin and 1% normal donkey serum for 15 minutes and blocked for 1 hour with a 5% donkey serum and 0.05% saponin. Primary antibodies utilized were goat anti-Olig2 (1:100, R&D Systems), mouse anti-CC1 (1:50, Millipore), mouse IgG2a anti-SOX2 (1:100, R&D Systems), mouse IgG1 anti-Ki67 (1:25, Fisher Scientific), rat IgG2a anti-MBP (1:300, Abcam Inc.), goat IgG Smi311 & Smi312 (1:1000, BioLegend), rabbit IgG anti-App (1:500, Thermo Fisher), rabbit IgG anti-Iba1 (1:300, Wako Chemicals), and mouse IgG1 anti-Gfap (1:400, Sigma-Aldrich). Alexa 488, 594, and 647-conjugated secondary antibodies (Invitrogen) were used at 1:500. Lesion areas were captured at 10X, 20X, and 60X magnification using an Olympus IX83 with IX3-SSU motorized stage and image tiles stitched via cellSens software. Images of immunostained sections were aligned with their corresponding FluoroMyelin stained section to accurately mark

229 lesion boundaries, with exclusion of any portion of the lesion which extends into the gray matter.
230 Cell counts were determined via a semi-automated, machine learning assisted, counting process
231 (code available upon request). The Keras based convolution network was trained on a set of
232 ~3250 CC1 positive and ~3250 CC1 negative pre-classified images (supervised learning).

233 *Fluorescence in situ hybridization*

234 Fluorescence in situ hybridization was performed with probes targeting Prrx1 (GenBank
235 accession #NM_011127.2) mRNA by using the RNAscope Fluorescent Multiplex Detection Kit
236 (Advanced Cell Diagnostics) according to the manufacturer instructions and as described
237 previously (Wang et al., 2018, Saraswat et al., 2021a). Fixed sections were baked at 60°C for 30
238 minutes, washed with ethanol, tissue pretreatment with proprietary buffers. Probes were then
239 hybridized and fluorescent conjugated. Sections were counterstained with DAPI to visualize
240 nuclei. Positive signals were identified as punctate dots present in nucleus and cytoplasm.

241 *Statistics*

242 All statistical testing was completed using GraphPad Prism Version 8.4.0. The control group for
243 all analyses of cell numbers and phenotypes was normal white matter (NWM) from uninjured
244 animals, or normal appearing white matter (NAWM) from a region distant from the lesion. Groups
245 comprised either time-points following injection of lysolecithin, regional analysis within the lesion,
246 or small vs large volume lesions. For all reporting, an experimental unit comprised a single lesion.
247 A minimum of 4 experimental units (lesions) per group was set *a priori*, along with a requirement
248 for at least three animals per group. Criteria for lesion inclusion were established *a priori*. Only
249 lesions located within internal capsule white matter were included in the analysis. No white matter
250 lesions regardless of size were excluded from the analysis. Rabbits were allocated to each group
251 in a randomized fashion based on availability from the vendor and surgical schedule.
252 Experimental units for large and small lesion animals are displayed in **Table 1**. Experimental units
253 for normal uninjured animals: 6 hemispheres, 3 animals. Total animals involved in the study, 38.
254 Manual cell count validations for all quantitative measures were performed in a blinded fashion.
255 Normality of data was tested in GraphPad using the D'Agostino-Pearson omnibus test. For
256 analysis of time-series data, one-way ANOVA with Tukey's post-hoc testing was performed. For
257 analysis of time-series and region/volume delimited data, two-way ANOVA with Sidak's post-hoc
258 testing was performed. Pairwise post-hoc testing was only performed if supported by ANOVA.
259 Only a portion of pairwise comparisons were highlighted, however full pairwise statistical
260 comparisons are available upon request.

Data availability

The data that supports the findings of this study are available upon reasonable request.

263 **RESULTS**

264 **Large lysolecithin-induced lesions in the rabbit persisted for at least 180 days.**

265 To test the hypothesis that supernumerary densities of OPCs are required for efficient
266 remyelination we sought to characterize OPC dynamics in a model of inefficient remyelination.
267 Lysolecithin-induced lesions in the sizable white matter tracts of the rabbit have been noted to
268 persist for at least 180 days (6 months) (Blakemore, 1978, Foster et al., 1980, Waxman et al.,
269 1979). To induce demyelination, we stereotactically injected lysolecithin into the periventricular
270 white matter of adult New Zealand White rabbits (bilateral injections of 1% lysolecithin, 5 µl) (**Fig.**
271 **1A**). We first examined lesion formation at 14 days post lesion (dpl). Overlay of a mouse coronal
272 section included for size reference. Lysolecithin induced focal demyelination at the site of injection
273 and resulted in a clearly demarcated region of hypercellularity that precisely matched the region
274 of myelin loss (**Fig. 1B**, white dashed line). The mean maximal cross-sectional area (MCA) and
275 volume were greatest at early time points and significantly declined with time (volume: 14 vs 21
276 dpl, Tukey's p = 0.032; MCA: 14 vs 56 dpl, Tukey's p = 0.013) (**Fig. 1C-D**). Large regions of
277 demyelination persisted in the rabbit even at 180 dpl. Volumetric analysis by serial section
278 reconstruction of the lesion indicated a comet-like appearance with a relatively spherical region
279 of demyelination corresponding to the site of injection and a tapered region extending in the
280 posterior-ventral direction (**Fig. 1E**).

281 **Insufficient OPC repopulation in the rabbit was associated with slow and incomplete OL**
282 **generation.**

283 We next sought to characterize the population dynamics of OPCs and OLs following
284 demyelination in the rabbit brain (**Fig 2**). We used Olig2 to label the entire oligodendrocyte lineage
285 and coexpression of CC1 and Olig2 to label post-mitotic OLs (**Fig. 2A**). Following demyelination,
286 Olig2$^+$ cell density was significantly reduced more than three-fold at 7 dpl (NWM vs 7 dpl, Tukey's
287 p < 0.0001) and never exceeded that of normal white matter (NWM) thereafter (**Fig. 2B**). The
288 density of OPCs/immature oligodendrocytes, defined as CC1$^-$Olig2$^+$ cells, significantly increased
289 between 7 and 14 dpl and remained stable at later time points (7 dpl vs 14 dpl; Tukey's p = 0.009)
290 (**Fig. 2C**). Following lysolecithin injection, the lesion was essentially devoid of OLs at 7 dpl (NWM
291 = 877.8 ± 62 vs 7 dpl = 79.9 ± 14 cells/mm^2) (**Fig. 2D**). By 56 dpl, OL density had partially
292 recovered and reached a plateau but remained significantly reduced at nearly half that of NWM
293 at 56 dpl (NWM = 877.8 ± 62 vs. 56 dpl = 453.9 ± 64.65 cells/mm^2, Tukey's p < 0.0017). The
294 proportion of CC1$^+$ OLs amongst the Olig2$^+$ population has been used to infer the rate of OL
295 differentiation. Intriguingly, while the proportion of OLs significantly increased with time until 21

296 dpl (7 dpl vs 21 dpl; Tukey's p = 0.009) (**Fig. 2E**), the proportion of OLs did not increase at later
297 time points suggesting that on-going OL generation may not continue after this initial period. The
298 percentage of $CC1^+$ OLs among total Olig2 remained low at 180 dpl indicating a chronic change
299 in oligodendrocyte lineage homeostasis (NWM = 66.3 ± 3.2% vs 180 dpl = 42.2 ± 9.1%). Together,
300 these data suggest that OPC repopulation in the rabbit lesions occurring following demyelination
301 is insufficient to generate sufficient OLs necessary to repair these lesions.

302 **OPC activation and proliferation were impaired following demyelination in the rabbit.**
303 Insufficient OPC recruitment in the rabbit may result from a failure of parenchymal OPCs to
304 respond appropriately to environmental signals associated with demyelination, and could result
305 from a disruption of OPC migration, activation, and/or proliferation. While we lacked the ability to
306 directly measure migration, we instead assessed OPC activation and proliferation. The
307 transcription factor Sox2 is upregulated in activated adult OPCs following demyelination and is
308 necessary for OPC recruitment and successful remyelination (Zhao et al., 2015). As expected, in
309 normal rabbit white matter the majority of $Olig2^+$ cells were $Sox2^-$ and $Ki67^-$ (**Fig. 3A**). Following
310 demyelination, recruited OPCs progressively upregulated Sox2, such that the majority of $Olig2^+$
311 cells in the lesion area coexpressed Sox2 by 14 dpl (NWM = 3.2 ± 2%, 14 dpl = 51.4 ± 3%) (**Fig.**
312 **3B**). Overall, the density of $Sox2^+Olig2^+$ OPC peaked at 14 dpl (NWM vs 14 dpl, 14 dpl vs 180
313 dpl, Tukey's $p < 0.0001$ and $p < 0.0001$, respectively), and returned to control levels by 180 dpl
314 (NWM vs 180 dpl, Tukey's $p > 0.05$) (**Fig. 3B-E**). The pattern of $Sox2^+$ expression among OL
315 lineage cells largely corresponded with their proliferative capacity defined by Ki67 expression.
316 The proportion of $Ki67^+$ cells among the $Olig2^+$ population peaked at 14 dpl and returned to
317 baseline by 180 dpl (NWM vs 14 dpl, 14 dpl vs 180 dpl, Tukey's p = 0.004 and p = 0.02,
318 respectively) (**Fig. 3B-D, F**). Interestingly, the proportion of dividing $Sox2^+Olig2^+$ remained
319 elevated until 56 dpl but never exceeded 30% (NWM vs 56 dpl, Tukey's p = 0.025) (**Fig. 3G**).
320 Together, this indicates a protracted period of OPC activation, whereby OPC proliferation fails to
321 keep pace, and one that ultimately fails to result in supernumerary OPC repopulation.

322 **Microglial/macrophage response correlates with the pattern of OPC repopulation**
323 Next, we examined the microglial and astrocyte response following demyelination to determine
324 whether the failure to recruit supernumerary OPCs could be attributed to the pattern of the innate
325 immune response. In this regard, we noted substantial upregulation of Sox2 among Olig2
326 negative cells following demyelination (**Fig. 3B-D**). We confirmed that these $Sox2^+$ cells were
327 largely reactive $Gfap^+$ astrocytes that were concentrated within the center of the demyelinated
328 lesion (**Fig. 3H**). A substantial number of $Sox2^+Olig2^-$ cells were observed within the lesion at all

329 time points, with statistically greatest numbers at 56 dpl followed by a reduction at 180 dpl (NWM
330 vs 56 dpl, 56 dpl vs 180 dpl, Tukey's $p = 0.045$ and $p = 0.018$, respectively) (**Fig. 3I**).
331 At 7 dpl, both microglial (Iba1) and astrocyte (Gfap) markers were upregulated throughout
332 the demyelinated lesion with a relatively homogenous pattern throughout the lesion area (**Fig.**
333 **4A**). At higher magnification, Iba1$^+$ microglia largely adopted an ameboid morphology while
334 astrocytes were hypertrophic and reactive in appearance (**Fig. 4A**, insets). At later timepoints
335 both microglia/macrophage and astrocyte signals were more concentrated toward the lesion
336 center (**Fig. 4B-D**). While Gfap immunoreactivity remained elevated through 180 days, Iba1 was
337 more transient with a peak between 7-14 days. Consistent with this qualitative assessment, Iba1
338 mean florescent intensity (MFI) peaked at 7 and 14 days and was significantly elevated relative
339 to normal appearing white matter (**Fig. 4E**) (NAWM; defined as matched uninjured corpus
340 callosum from the same cohort of animals, n=29). Iba1 was elevated relative to NAWM at early
341 time points up to and including 56 dpl (NAWM vs 56 dpl, Tukey's $p = 0.006$). However, Iba1
342 staining was reduced at 180 dpl (7 dpl vs 180 dpl, Tukey's $p < 0.0001$) (**Fig. 4E**). In contrast, the
343 astrocytic response defined by Gfap area remained significantly elevated throughout the
344 experimental time course, with significant Gfap upregulation vs. NAWM still apparent at 180 dpl
345 (NAWM vs 180 dpl, Tukey's $p = 0.02$) (**Fig. 4F**). Gfap upregulation was stable as no significant
346 pairwise differences were observed between 7 dpl and any later timepoint (Tukey's $p > 0.05$).
347 Consistent with these observations, the total density of DAPI$^+$ nuclei in the lesion area peaked at
348 14 dpl and declined thereafter. DAPI$^+$ density was significantly decreased 56 vs. 14 dpl (Tukey's
349 14 vs 56 dpl, $p = 0.04$) (**Fig. 4G**). Together, these results suggest that astroglial and microglial
350 responses are distinct from one another and, intriguingly, that the overall microglial rather than
351 the astroglial response corresponded to the pattern of OPC activation and proliferation.
352 Interestingly, in the center of the lesion ameboid microglia/macrophages commonly
353 formed vesicular structures which were observed at early 14 dpl (**Fig. 5A**), and later 56 dpl
354 timepoints (**Fig. 5B**). These structures overwhelmingly represent myelin ladened
355 microglia/macrophages, which were also present at 56 dpl, albeit at lower number (**Fig. 5C-E**).
356 Additionally, while almost all of these vesicular Iba1$^+$ structures were ladened with myelin at 14
357 dpl, there were a significant portion at 56 dpl which did not demonstrate immunoreactivity to
358 myelin debris or neurofilament (**Fig. 5D-E**). As myelin debris impairs remyelination (Kotter et al.,
359 2006), these data suggest that inefficient myelin clearance in the lesion core may influence repair
360 in the rabbit.

361 **Large rabbit lesions display regional differences in cellularity, demyelination, and axonal**
362 **loss.**
363 Toxin-induced demyelination in mouse models is characterized by a region of hypercellularity
364 which corresponds to the extent of myelin degeneration. We compared the extent of myelin loss
365 defined by FluoroMyelin (FM) with the relative density of $DAPI^+$ nuclei between 7 and 180 dpl
366 (**Fig. 6**). The region of demyelination, defined by loss of FM staining, was hypercellular at 7 dpl
367 (**Fig. 6A**) and remained so thereafter. However, surrounding the region of demyelination (**Fig. 6A,**
368 white dashed line), we also observed a region of mild hypercellularity compared to that of more
369 distant white matter (**Fig. 6A'**, blue dashed line). We termed this region perilesion white matter
370 (PLWM) and confirmed via quantitative analysis that the cell density was significantly elevated
371 compared to distant NAWM (Tukey's p = 0.0002) (**Fig. 6B**). We next examined the relative area
372 of the demyelinating lesion and the associated PLWM with respect to time. Interestingly, while
373 the area of PLWM was smaller than the demyelinated lesion at earlier timepoints, the PLWM area
374 exceeded that of the lesion by 56 dpl and further expanded at 180 dpl (**Fig. 6C**). To investigate
375 the potential cellular identity of cells within the PLWM, we quantified the intensity of microglial and
376 astrocytic staining in the PLWM compared to distant NAWM. At 21 dpl, the PLWM exhibited
377 significantly increased staining for both Iba1 and Gfap consistent with an increased number of
378 both microglia/macrophages and astrocytes (**Supplemental Fig. 1**).
379 Next, we confirmed demyelination using myelin basic protein (Mbp) immunofluorescence
380 that corresponded with the loss of FM staining. Compared to myelin fiber staining in NAWM (**Fig.**
381 **6D**), abundant Mbp^+ myelin debris was observed at 7 dpl (**Fig. 6F/6F'**). The amount of myelin
382 debris was substantially reduced by 21 dpl. By 56 dpl, there was a partial recovery of Mbp
383 immunoreactivity within the lesion, but this was clearly distinct from NAWM (**Fig. 6F, 56 dpl**).
384 Within the PLWM, we did not observe myelin debris at earlier timepoints (7 and 21 dpl), and the
385 pattern and intensity of staining closely resembled NAWM. However, at 56 and 180 dpl we
386 observed subtle changes in the PLWM with reduced Mbp intensity and uneven staining.
387 Consistent with primary demyelination, neurofilament (NF)-labelled axons were observed
388 at all time points in the lesion (**Fig. 6G, Supplemental Fig. 2**). The center of the large rabbit lesion
389 displayed a small area of localized axonal loss (9-13% of total lesion area) that remained stable
390 in size thereafter (**Supplemental Fig. 2G**). Consistent with the loss of axons in the lesion center,
391 we observed accumulation of App immunoreactivity specifically at 7 dpl which disappeared at
392 later time points (**Fig. 6G'**).

Rabbit lesions exhibit region specific gradients of OPC activation and OL differentiation. The distribution and transcriptional profile of OPCs and OLs have been shown to be dependent on their location within the lesion (e.g., core & periphery) (Boyd et al., 2013, Absinta et al., 2021). The larger rabbit lesions allowed for correlation between OPC density and the local gliotic response in specific intra-lesional regions. The lesion edge was defined as the 75 μm wide band extending into the region of demyelination from the lesion border, the remainder of the lesion will be hereafter referred to as lesion core. We examined OPC density and differentiation in each region (**Fig. 7A-E**). The lesion core and lesion edge displayed similar amounts of hypercellularity, with lesser amount of cellularity in the PLWM (**Fig. 7A**). We observed a reduction in OL density ($CC1^+Olig2^+$) that corresponded to location within the lesion, such that OL density was lowest in the lesion core and was significantly greater in the PLWM (Two-way ANOVA, region; $F(2,56) = 10.72$, $p = 0.0001$) (**Fig. 7B, 7F**). Consistent with a failure to repair regardless of region, the density of OLs in the PLWM remained significantly depressed relative to normal white matter (unpaired t test, two-tailed, NWM = 877.8 ± 62 vs PLWM at 180 dpl = 591.7 ± 110, $p = 0.048$).

Rabbit lysolecithin lesions exhibited the greatest $Olig2^+CC1^-$ defined OPC density in the lesion core with progressively lower densities of OPCs observed in lesion edge and PLWM regions respectively (Two-way ANOVA, region; $F(2,56) = 7.15$, $p = 0.0017$) (**Fig. 7G**). The inverse pattern of OPC and OL density suggests region specific regulation of differentiation. We quantitatively examined the axonal density in lesion edge and core (**Supplemental Fig. 2H**). As expected, the lesion edge had significantly higher axonal density than core and corresponded with the inverse relationship of OPC and OL densities in these regions (Two-way ANOVA, region; $F(1,30) = 21.0$, $p < 0.0001$).

As successful remyelination in animal models is correlated with excess production of OPCs, we sought to determine why OPC density never exceeded that of NAWM in the lesion edge. Transient upregulation of $Sox2^+$ by activated OPCs is required for remyelination (Zhao et al., 2015). We examined the proportion of $Sox2^+$ activated $Olig2^+$ cells in each region following demyelination (**Fig. 7C**). We observed the greatest proportion of $Sox2^+$ OPCs in the lesion core (Two-way ANOVA, region; $F(2,51) = 4.22$, $p = 0.02$) (**Fig. 7H**). The proportion of $Sox2^+$ OPCs among $Olig2^+$ cells peaked at 14 dpl and declined thereafter. The relatively slow onset of Sox2 expression among rabbit OPCs suggested that other mechanisms may prevent OPC activation and proliferation at earlier time points.

Pathological OPC quiescence may contribute to failed differentiation in the lesion edge.

We have previously shown that human OPCs overexpressing the transcription factor Prrx1 enter a reversible state of quiescence that prevents their cell-cycle entry and limits their capacity to myelinate host shiverer axons (Wang et al., 2018). Similar to previous reports, following induction of demyelination Prrx1 expression was found in both Olig2$^+$ oligodendrocyte lineage and other Olig2$^-$ cells (**Fig. 7I-J**). We noted a striking accumulation of Prrx1 expressing Olig2$^+$ cells in the lesion edge at 14 dpl (**Fig. 7I**). This was a transient phenomenon as the density and percentage of Prrx1$^+$Olig2$^+$ cells decreased significantly by 56 dpl (**Fig. 7J-L**). The accumulation of Prrx1$^+$Olig2$^+$ cells at the lesion edge suggests that OPCs entering the demyelinated region rapidly upregulated Prrx1 and likely become quiescent, thereby reducing their capacity to sufficiently repopulate the lesion. Consistent with altered OPC signaling in the rabbit, we observed occasional cytoplasmic Olig2 staining in the majority of sections analyzed with cells specifically localized around the edge of the lesion (**Fig. 7M**). The appearance of cytoplasmic Olig2 has been previously attributed to cells transitioning to an astroglial fate via IFN-γ (Cassiani-Ingoni et al., 2006).

Small volume lesions exhibited similar astrogliosis but relatively reduced microglial/macrophage responsiveness.

We next asked whether the deficits in OPC proliferation and differentiation could be attributed to lesion volume alone. We created small volume lesions via injection of 0.35 μL lysolecithin. Small volume lesions were 7-fold smaller by volume than large volume rabbit lesions, and closely resembled the volume of murine lesions (Kucharova et al., 2011) (murine lesions = 0.4 mm^3, small volume rabbit = 0.39 $\pm$ 0.1 mm^3, large volume rabbit = 3.6 $\pm$ 0.3 mm^3) (n=4 and 8, respectively) (**Fig. 8A-F, 8G**). Similar to large rabbit lesions, small volume lesions displayed equivalent levels of hypercellularity and astrogliosis (Gfap) compared to large volume lesions (**Fig. 8A-B, 8D-E**). Indeed, there were no significant differences between small and large volume lesions at any time point in terms of DAPI or GFAP (**Fig. 8H-I**). Intriguingly, we noted that small volume lesions had less intense Iba1 staining compared to large lesions (**Fig. 8C, 8F**) (Two-way ANOVA, volume: $F(1,28) = 17.39$, $p = 0.0003$). Mean Iba1 intensity was significantly decreased relative to large volume lesions at both 7 and 14 dpl (Sidak $p = 0.0015$ and 0.013, respectively) (**Fig. 8J**). Unlike larger volume lesions (1 and 5 μl), we did not observe a central region of axonal loss following injection of 0.35 μl lysolecithin (**Supplemental Fig. 2**). Axonal loss in small lesions was equivalent to that of the large lesion edge (**Supplemental Fig. 2I**).

455 **OPC activation and proliferation was substantially reduced in small rabbit lesions.**
456 To determine whether OPC repopulation was altered in small volume lesions, we interrogated
457 activation and proliferation of OPCs using Sox2 and Ki67, respectively (**Fig. 9**). We compared the
458 density of cells within the small lesion to the lesion edge of large volume lesions to exclude any
459 effects of the central region of axonal loss. The overall density of Olig2$^+$ cells following
460 demyelination was similar between large and small lesions (Two-way ANOVA, volume;
461 $F(1,22)=3.73$, $p > 0.05$) (**Fig. 9A, 9E**). However, unlike other animal models of spontaneous
462 remyelination, Olig2 density within the demyelinated lesion never exceeded that of normal
463 uninjured white matter regardless of lesion volume (dotted line).
464 Examination of Sox2 and Ki67 revealed far more apparent volume-dependent effects (**Fig.**
465 **9B-C**). The density of Sox2$^+$Olig2$^+$ cells was significantly lower in small vs. large lesions following
466 demyelination (Two-way ANOVA, volume; $F(1,21) = 24.38$, $p < 0.0001$). At 14 dpl, the extent of
467 Sox2 activation was >2-fold decreased in small lesions (Sidak's $p = 0.0003$) (**Fig. 9F**). This
468 corresponded with a profound reduction in the proportion of actively proliferating Ki67$^+$ OPCs
469 across time points (Two-way ANOVA, volume; $F(1,21) = 20.05$, $p = 0.0002$) (**Fig. 9G**). As Olig2
470 expression is maintained in OLs, we next examined the fraction of Ki67$^+$ cells among Sox2$^+$Olig2$^+$
471 activated OPCs (**Fig. 9H**). Very few, <1%, of these OPCs expressed Ki67 suggesting that OPC
472 proliferation is highly dependent on lesion volume in the rabbit and suggests that OPC
473 repopulation in small rabbit lesions is principally due to migration from NAWM.
474 Although proliferation was substantially lower in small volume lesions, there was
475 surprisingly no significant difference in the density of CC1$^-$Olig2$^+$ OPCs between small and large
476 volume lesions (Two-way ANOVA, volume; $F(1,22) = 0.25$, $p > 0.05$) (**Fig. 9I**). Large lesions with
477 7-fold greater volume requires approximately 2-3 more cell divisions to achieve the same density
478 of OPCs. The generation of CC1$^+$ OLs was not significantly different between small lesions and
479 the edge of large lesions (CC1$^+$Olig2$^+$ cell density; Two-way ANOVA, volume; $F(1,22) = 3.45$, $p >$
480 0.05) (**Fig. 9D, 9J**). Likewise, the rate of OL generation was equivalent between small and large
481 lesions (Two-way ANOVA, volume; $F(1,22) = 1.81$, $p > 0.05$) (**Fig. 9K**). These results suggest
482 that OPC activation and proliferation is highly influenced by lesion volume in the rabbit. Together,
483 these contribute to a failure to coordinate OPC recruitment with differentiation and together lead
484 to chronic demyelination.

485 **DISCUSSION**

486 Unlike murine models, spontaneous remyelination is inefficient in rabbit models with chronic
487 demyelination persisting at least 6 months following injection of lysolecithin (Blakemore, 1978,
488 Foster et al., 1980), and following induction of experimental autoimmune encephalomyelitis (EAE)
489 (Williams et al., 1982, Prineas et al., 1969). Although reported over 40 years ago, the mechanisms
490 underlying the failure of rabbit remyelination have not been investigated. Here, we show that the
491 OPC response to demyelination is fundamentally altered in the rabbit brain relative to typically
492 employed rodent models. In most rodent models, OPC density far exceeds that of normal white
493 matter during the recruitment phase of remyelination. In contrast, rabbit OPC density slowly
494 recovers following demyelination but never exceeds that observed in normal white matter.
495 Deficient OPC proliferation and subsequently poor OPC repopulation in large rabbit lesions was
496 associated with an upregulation of quiescence-associated genes and this corresponded with
497 delayed and insufficient oligodendrocyte (OL) generation. In contrast, small rabbit lesions were
498 essentially devoid of dividing OPCs and did not efficiently upregulate Sox2 in response to
499 demyelination. As OPC repopulation was reduced in rabbit small lesions compared to mouse
500 lesions of equivalent size, our results also highlight the potential importance of species-dependent
501 differences in the response to demyelination (Dietz et al., 2016).

502 Parenchymal adult OPCs retain the capacity to generate new OLs and are largely
503 considered to be the primary source of newly generated OLs following demyelination in the adult
504 CNS (Serwanski et al., 2018, Zawadzka et al., 2010). In mouse models of toxin-induced
505 demyelination and EAE, the OPC recruitment phase of remyelination is not typically rate limiting
506 (Franklin and Goldman, 2015). Furthermore, approaches to improve OPC recruitment have not
507 meaningfully altered the rate of myelin regeneration in focal mouse lesions. For example,
508 overexpression of PDGF-AA drives enhanced OPC recruitment following demyelination and yet
509 this had no discernable effect on the rate of remyelination (Woodruff et al., 2004). The progenitor
510 pool in small rodent models is especially capable of efficient recruitment and occurs following
511 systemic depletion either by X-irradiation (Chari and Blakemore, 2002) or pharmacogenetic
512 depletion (Xing et al., 2021) and, importantly, after demyelination. Repeated focal demyelination
513 is not sufficient to deplete the progenitor pool (Penderis et al., 2003) and only sustained depletion
514 of OL lineage cells using 12-week treatment can prevent efficient remyelination in the cuprizone
515 model (Mason et al., 2004). The relative success of OPC recruitment in the mouse is exemplified
516 by the rapid regeneration of OPCs following demyelination, with a 2-3 fold increase in density
517 over normal white matter (Sim et al., 2002, Ulrich et al., 2008, Kucharova and Stallcup, 2015, Lin
518 et al., 2006). In contrast, rabbit lesions regardless of size are characterized by a failure of OPC

519 repopulation such that the density of OPCs never exceeds that of normal tissue and the
520 characteristic over-population of OPCs that occurs in the mouse and rat is absent. The rate of
521 OPC repopulation is also comparatively delayed, reaching peak density only after 14 days.
522 Whereas mouse and rats reach peak progenitor density within the first week (Sim et al., 2002,
523 Fancy et al., 2004). While the dynamics of OPC recruitment in humans is difficult to ascertain
524 from postmortem tissue, MS lesions rarely display OPC densities that exceed that of NAWM
525 (Lucchinetti et al., 1999, Kuhlmann et al., 2008, Boyd et al., 2013, Moll et al., 2013, Tepavcevic
526 et al., 2014). Demyelination of the optic nerve in non-human primates similarly lacks the abundant
527 recruitment of OPCs that is observed in murine models, with densities of OPCs and OLs not
528 recovering until 9 months after injection of lysolecithin (Sarrazin et al., 2022). Fascinatingly, even
529 at 9 months when OLs and OPC densities have recovered, few axons show evidence of
530 remyelination (Sarrazin et al., 2022). Together these data suggest that OPC recruitment in the
531 rabbit model more closely resembles that observed in MS and non-human primates.

532 While our data identify a substantial deficit in the ability of rabbit OPCs to repopulate
533 regions of demyelination, we also noted a relative failure in the ability of OPCs to undergo
534 differentiation. We observed a substantial decrease in the proportion of $CC1^+$ OLs among the
535 entire $Olig2^+$ lineage relative to mouse/rat model systems. In the lesion core, we observed fewer
536 OLs compared to other regions, and this corresponded with increased expression of markers of
537 tissue injury (including OPC, microglial, and astrocytic activation and axonal loss). Together, this
538 suggests the presence of a proinflammatory environment in the lesion core that contribute to failed
539 OL differentiation. An alternative hypothesis is that the failure of recruitment itself contributes to
540 failed differentiation. *In vitro* OL differentiation is dependent on the density of OPCs (Rosenberg
541 et al., 2008) and, similarly, following transplantation human OL differentiation is correlated with
542 the local density of human OPCs (Dietz et al., 2016). This suggests that below a certain threshold
543 local density of OPCs, the process of OL differentiation itself may be limited. Consistent with this
544 hypothesis, remyelinated lesions and active lesions in MS, which have a higher propensity for
545 remyelination, tend to have higher densities of OPCs than chronic demyelinated lesions (Boyd et
546 al., 2013). Lastly, at least within the central region of axonal loss, the failure of OL differentiation
547 may be due to the absence of an appropriate axonal substrate. This might also account for the
548 low density of OLs and relatively high density of OPCs found in the lesion core of large rabbit
549 lesions. Likewise, lysolecithin-induced lesions of non-human primate optic nerve induced
550 widespread axonal loss similar to the central region of axonal loss in the rabbit and display
551 similarly low densities of OLs (Sarrazin et al., 2022). However, axonal loss is unlikely to explain
552 the reduced density of OLs observed in edge of large rabbit lesions or across small volume lesions

553 where axonal loss is not as apparent. Chronic demyelination is observed following injection of 2.5
554 – 5 μL lysolecithin into the rabbit spinal cord at 6 months (Blakemore, 1978). While this is likely
555 recapitulated in this study (brain, 5 μL), it is possible that remyelination is more efficient in small
556 (0.35 μL) lesions or those localized to the cerebral white matter. It is worth noting that the density
557 of OLs in small lesions was not significantly greater than the lesion edge of large lesions and
558 reduced myelin content assessed by fluoromyelin remained evident at 21 dpl suggesting a similar
559 outcome. However, future ultrastructural analyses will be needed to elucidate this.

560 Several pieces of evidence in the current study point toward the importance of species
561 differences in OPC recruitment. Contrary to our initial hypothesis, the recovery of OPC density in
562 small volume lesions (0.4 mm^3) was not improved relative to large volume (4.0 mm^3) lesions and
563 the peak density of OPCs was unaffected by lesion volume. This suggests that lesion volume is
564 not the principal determinant of OPC recruitment. In contrast, OPC autonomous differences were
565 apparent between the rabbit and mouse. Sox2 is upregulated by OPCs following demyelination
566 in the mouse brain and is necessary for precursor proliferation (Zhao et al., 2015). On the other
567 hand, downregulation of Sox2 is required for subsequent differentiation. In murine models, Sox2
568 is rapidly upregulated in the majority of OPCs within a week of lesion formation. In contrast, OPCs
569 in the rabbit are slow to upregulate Sox2, failing to peak for at least 14 days. Sox2 expression
570 persists for several weeks in the rabbit but is not associated with continued OPC proliferation
571 suggesting a pathologic state of OPC activation. Furthermore, the transcriptional regulator Prrx1,
572 a transcription factor associated with OPC quiescence (Wang et al., 2018), was specifically
573 upregulated in numerous rabbit OPCs located at the lesion border. Prrx1 induces a reversible
574 state of quiescence inhibiting proliferation and thereby preventing efficient myelination (Wang et
575 al., 2018). Prrx1 itself is regulated by both interferon-γ and BMP signaling (Wang et al., 2018,
576 Saraswat et al., 2021b) and increased Prrx1 expression in the rabbit suggests that the lesion
577 environment may differ substantially from the mouse brain. Intriguingly, we also observed
578 prominent examples of cells expressing cytoplasmic Olig2 expression in the rabbit lesion that is
579 associated with an astroglial switch in stem/progenitor cells (Setoguchi, 2004) and observed in
580 rare cells in EAE (Cassiani-Ingoni et al., 2006). This is not observed in mouse lysolecithin lesions
581 and further supports species-specific differences in signaling. OPC autonomous differences
582 between species have been suggested by several other studies. For example, adult mouse OPCs
583 are more than twice as migratory compared to adult human OPCs (Bribian et al., 2020). Following
584 transplantation, human OPCs take 8-12 weeks to generate myelin-forming OLs (Sim et al., 2011,
585 Windrem et al., 2004, Windrem et al., 2008, Buchet et al., 2011), while equivalent rodent cells
586 typically complete the process of differentiation in 3-4 weeks (Baron-Van Evercooren and

587 Blakemore, 2004). Lastly, when human OPCs are transplanted into mouse brain, the human cells
588 outcompete their mouse counterparts suggestive of substantial differences in cell biology and
589 signaling between species (Windrem et al., 2014). Together, these results support the hypothesis
590 that species differences are critical determinants of the OPC response to demyelination.

591 Our analysis of small and large rabbit lesions revealed interesting differences in the
592 progenitor response to demyelination. The edge of large lesions and small lesions demonstrated
593 similar densities of OPC and OLs at every timepoint studied. Unlike large lesions, Ki67^{+} OPCs
594 were rarely observed in small lesions suggesting that the rate of proliferation was substantially
595 less and strongly influenced by the amount of tissue injury. In the current study, we could not
596 directly measure the contribution of migration to the general failure of OPC recruitment. However,
597 as we observed a similar density of cells in small and large lesions but with the absence of
598 proliferation in small lesions, this implies that OPC repopulation in small lesions may have been
599 largely dependent on migration from surrounding tissue rather than local expansion. This
600 corresponded with a much lower level of Sox2-expression amongst OPCs in small lesions and
601 suggests an altered transcriptional state dependent on lesion volume. In addition to volume-
602 dependent differences in the progenitor response, we also observed differences within individual
603 lesion such that significantly higher densities of OPCs were observed in the lesion core.
604 Proliferating Sox2^{+}Olig2^{+} cells were also largely found in the lesion core and this corresponded
605 with enhanced Iba1 and Gfap staining suggesting that the gliotic core was in part driving the
606 sustained OPC proliferation observed in that region. In contrast, we found increased generation
607 of OLs at the lesion border, a pattern commonly found in MS (Hess et al., 2020). The potential
608 mediators of these differences are outside the scope of the current study but further support the
609 importance of the local environment in the determination of OPC state and its capacity for both
610 proliferation and differentiation.

611 In summary, the rabbit model provides evidence for both species and volume dependent
612 effects on the cellular mechanisms of remyelination. Unlike mouse/rat models in which OPC and
613 oligodendrocyte densities far exceed normal white matter densities following demyelination, in the
614 rabbit these cells repopulate the lesion at a slower rate and never reach supernumerary densities.
615 When comparing mouse and rabbit lesions of equivalent size, we found that activation of Sox2
616 occurs more slowly, and that proliferation is almost absent in the rabbit. These processes are
617 themselves volume dependent as prolonged OPC proliferation and activation occurs in large
618 volume rabbit lesions. The failure of OPC proliferation, and subsequently OPC recruitment, in the
619 rabbit recapitulates the extent of OPC recruitment commonly observed in the majority of MS
620 lesions, as well as non-human primates, and thereby provides a suitable test bed for therapeutic

approaches aimed at improving the migration and proliferation of OPCs. As such, we propose that the simplicity and accessibility of the rabbit model along with the clear differences in lesion environment and patterns of OPC recruitment and differentiation will provide a vital complementary approach for preclinical testing of remyelination therapeutics and aid in the successful development of clinical interventions aimed at promoting myelin regeneration.

Conflict of Interest: The authors declare no competing financial interests.

Author Contributions:

Conception and design of the study: FJS and JJMC. Acquisition and analysis of data: all authors. Drafting the manuscript or figures: FJS and JJMC. Study supervision: FJS.

631 **REFERENCES**

632 ABSINTA, M., MARIC, D., GHARAGOZLOO, M., GARTON, T., SMITH, M. D., JIN, J.,
633 FITZGERALD, K. C., SONG, A., LIU, P., LIN, J. P., WU, T., JOHNSON, K. R.,
634 MCGAVERN, D. B., SCHAFER, D. P., CALABRESI, P. A. & REICH, D. S. 2021. A
635 lymphocyte-microglia-astrocyte axis in chronic active multiple sclerosis. *Nature,* 597**,** 709-
636 714.

637 BACMEISTER, C. M., BARR, H. J., MCCLAIN, C. R., THORNTON, M. A., NETTLES, D., WELLE,
638 C. G. & HUGHES, E. G. 2020. Motor learning promotes remyelination via new and
639 surviving oligodendrocytes. *Nat Neurosci,* 23**,** 819-831.

640 BARON-VAN EVERCOOREN, A. & BLAKEMORE, W. F. 2004. Chapter 6 - Remyelination
641 through Engraftment. *In:* LAZZARINI, R. A., GRIFFIN, J. W., LASSMAN, H., NAVE, K.-A.,
642 MILLER, R. & TRAPP, B. D. (eds.) *Myelin Biology and Disorders.* San Diego: Academic
643 Press.

644 BLAKEMORE, W. F. 1978. Observations on remyelination in the rabbit spinal cord following
645 demyelination induced by lysolecithin. *Neuropathol Appl Neurobiol,* 4**,** 47-59.

646 BOYD, A., ZHANG, H. & WILLIAMS, A. 2013. Insufficient OPC migration into demyelinated
647 lesions is a cause of poor remyelination in MS and mouse models. *Acta Neuropathol,* 125**,**
648 841-59.

649 BRIBIAN, A., MEDINA-RODRIGUEZ, E. M., JOSA-PRADO, F., GARCIA-ALVAREZ, I., MACHIN-
650 DIAZ, I., ESTEBAN, P. F., MURCIA-BELMONTE, V., VEGA-ZELAYA, L., PASTOR, J.,
651 GARRIDO, L. & DE CASTRO, F. 2020. Functional Heterogeneity of Mouse and Human
652 Brain OPCs: Relevance for Preclinical Studies in Multiple Sclerosis. *J Clin Med,* 9.

653 BROWN, J. W. L., CUNNIFFE, N. G., PRADOS, F., KANBER, B., JONES, J. L., NEEDHAM, E.,
654 GEORGIEVA, Z., ROG, D., PEARSON, O. R., OVERELL, J., MACMANUS, D., SAMSON,
655 R. S., STUTTERS, J., FFRENCH-CONSTANT, C., GANDINI WHEELER-KINGSHOTT,
656 C. A. M., MORAN, C., FLYNN, P. D., MICHELL, A. W., FRANKLIN, R. J. M., CHANDRAN,
657 S., ALTMANN, D. R., CHARD, D. T., CONNICK, P. & COLES, A. J. 2021. Safety and
658 efficacy of bexarotene in patients with relapsing-remitting multiple sclerosis (CCMR One):
659 a randomised, double-blind, placebo-controlled, parallel-group, phase 2a study. *The*
660 *Lancet Neurology,* 20**,** 709-720.

661 BUCHET, D., GARCIA, C., DEBOUX, C., NAIT-OUMESMAR, B. & BARON-VAN
662 EVERCOOREN, A. 2011. Human neural progenitors from different foetal forebrain regions
663 remyelinate the adult mouse spinal cord. *Brain,* 134**,** 1168-83.

664 CADAVID, D., MELLION, M., HUPPERTS, R., EDWARDS, K. R., CALABRESI, P. A.,
665 DRULOVIĆ, J., GIOVANNONI, G., HARTUNG, H.-P., ARNOLD, D. L., FISHER, E.,
666 RUDICK, R., MI, S., CHAI, Y., LI, J., ZHANG, Y., CHENG, W., XU, L., ZHU, B., GREEN,
667 S. M., CHANG, I., DEYKIN, A., SHEIKH, S. I., AGÜERA MORALES, E., AL KHEDR, A.,
668 AMPAPA, R., ARROYO, R., BELKIN, M., BONEK, R., BOYKO, A., CAPRA, R.,
669 CENTONZE, D., CLAVELOU, P., DEBOUVERIE, M., DRULOVIC, J., EDWARDS, K.,
670 EVANGELOU, N., EVDOSHENKO, E., FERNÁNDEZ, O., FERNÁNDEZ SÁNCHEZ, V.,
671 FREEDMAN, M., FREEDMAN, S., FRYZE, W., GARCIA-MERINO, A., GAVRIC-KEZIC,
672 M., GHEZZI, A., GOUT, O., GRIMALDI, L., HENDIN, B., HERTMANOWSKA, H.,
673 HINTZEN, R., HRADILEK, P., HUPPERTS, R., ILKOWSKI, J., IVASHINENKOVA, E.,
674 IZQUIERDO, G., JACQUES, F., JAKAB, G., KHABIROV, F., KLODOWSKA-DUDA, G.,
675 KOMOLY, S., KOSTIC, S., KOVAROVA, I., KREMENCHUZKY, M., LAGANKE, C.,
676 LAPIERRE, Y., MACIEJOWSKI, M., MAISON, F. G., MARFIA, G. A., MARTÍNEZ
677 YÉLAMOS, S., MELUZINOVA, E., MONTALBAN, X., MURRAY, R., NAISMITH, R.,
678 NEWSOME, S., NGUYEN, V., OREJA, D., PARDO, G., PASECHNIK, E., PATTI, F.,
679 POTEMKOWSKI, A., PROKOPENKO, S., QIAN, P., RODRÍGUEZ-ANTIGÜEDAD, A.,
680 ROSSMAN, H., ROZSA, C., SÁNCHEZ LÓPEZ, F., SELMAJ, K., SILBER, E., STEPIEN,
681 A., STEPNIEWSKA, A., SWIAT, M., TONCEV, G., TOURBAH, A., TRUSHNIKOVA, T.,
682 UCCELLI, A., VACHOVA, M., VALIS, M., VECSEI, L., WIERTLEWSKI, S., ZAFFARONI,
683 M., et al. 2019. Safety and efficacy of opicinumab in patients with relapsing multiple
684 sclerosis (SYNERGY): a randomised, placebo-controlled, phase 2 trial. *The Lancet*
685 *Neurology,* 18**,** 845-856.

686 CASSIANI-INGONI, R., COKSAYGAN, T., XUE, H., REICHERT-SCRIVNER, S. A., WIENDL, H.,
687 RAO, M. S. & MAGNUS, T. 2006. Cytoplasmic translocation of Olig2 in adult glial
688 progenitors marks the generation of reactive astrocytes following autoimmune
689 inflammation. *Exp Neurol,* 201**,** 349-58.

690 CHARI, D. M. & BLAKEMORE, W. F. 2002. Efficient recolonisation of progenitor-depleted areas
691 of the CNS by adult oligodendrocyte progenitor cells. *Glia,* 37**,** 307-13.

692 DIETZ, K. C., POLANCO, J. J., POL, S. U. & SIM, F. J. 2016. Targeting human oligodendrocyte
693 progenitors for myelin repair. *Exp Neurol,* 283**,** 489-500.

694 DUNCAN, I. D., RADCLIFF, A. B., HEIDARI, M., KIDD, G., AUGUST, B. K. & WIERENGA, L. A.
695 2018. The adult oligodendrocyte can participate in remyelination. *Proc Natl Acad Sci U S*
696 *A,* 115**,** E11807-E11816.

697 FANCY, S. P., BARANZINI, S. E., ZHAO, C., YUK, D. I., IRVINE, K. A., KAING, S., SANAI, N.,
698 FRANKLIN, R. J. & ROWITCH, D. H. 2009. Dysregulation of the Wnt pathway inhibits
699 timely myelination and remyelination in the mammalian CNS. *Genes Dev,* 23**,** 1571-85.
700 FANCY, S. P., ZHAO, C. & FRANKLIN, R. J. 2004. Increased expression of Nkx2.2 and Olig2
701 identifies reactive oligodendrocyte progenitor cells responding to demyelination in the
702 adult CNS. *Mol Cell Neurosci,* 27**,** 247-54.
703 FOSTER, R. E., KOCSIS, J. D., MALENKA, R. C. & WAXMAN, S. G. 1980. Lysophosphatidyl
704 choline-induced focal demyelination in the rabbit corpus callosum. Electron-microscopic
705 observations. *J Neurol Sci,* 48**,** 221-31.
706 FRANKLIN, R. J. & GOLDMAN, S. A. 2015. Glia Disease and Repair-Remyelination. *Cold Spring*
707 *Harb Perspect Biol,* 7**,** a020594.
708 FRANKLIN, R. J. M. & FFRENCH-CONSTANT, C. 2017. Regenerating CNS myelin - from
709 mechanisms to experimental medicines. *Nat Rev Neurosci,* 18**,** 753-769.
710 GARAY, L., TUNGLER, V., DENISELLE, M. C., LIMA, A., ROIG, P. & DE NICOLA, A. F. 2011.
711 Progesterone attenuates demyelination and microglial reaction in the lysolecithin-injured
712 spinal cord. *Neuroscience,* 192**,** 588-97.
713 GREEN, A. J., GELFAND, J. M., CREE, B. A., BEVAN, C., BOSCARDIN, W. J., MEI, F., INMAN,
714 J., ARNOW, S., DEVEREUX, M., ABOUNASR, A., NOBUTA, H., ZHU, A., FRIESSEN,
715 M., GERONA, R., VON BÜDINGEN, H. C., HENRY, R. G., HAUSER, S. L. & CHAN, J. R.
716 2017. Clemastine fumarate as a remyelinating therapy for multiple sclerosis (ReBUILD):
717 a randomised, controlled, double-blind, crossover trial. *The Lancet,* 390**,** 2481-2489.
718 HESS, K., STAROST, L., KIERAN, N. W., THOMAS, C., VINCENTEN, M. C. J., ANTEL, J.,
719 MARTINO, G., HUITINGA, I., HEALY, L. & KUHLMANN, T. 2020. Lesion stage-dependent
720 causes for impaired remyelination in MS. *Acta Neuropathol,* 140**,** 359-375.
721 HUANG, J. K., JARJOUR, A. A., FFRENCH-CONSTANT, C. & FRANKLIN, R. J. 2011. Retinoid
722 X receptors as a potential avenue for regenerative medicine in multiple sclerosis. *Expert*
723 *Rev Neurother,* 11**,** 467-8.
724 HUGHES, E. G., KANG, S. H., FUKAYA, M. & BERGLES, D. E. 2013. Oligodendrocyte
725 progenitors balance growth with self-repulsion to achieve homeostasis in the adult brain.
726 *Nat Neurosci,* 16**,** 668-76.
727 JEAN, I., LAVIALLE, C., BARTHELAIX-POUPLARD, A. & FRESSINAUD, C. 2003. Neurotrophin-
728 3 specifically increases mature oligodendrocyte population and enhances remyelination
729 after chemical demyelination of adult rat CNS. *Brain Res,* 972**,** 110-8.

730 KOHLER, C., WAHL, H., ZIEMSSEN, T., LINN, J. & KITZLER, H. H. 2019. Exploring individual
731 multiple sclerosis lesion volume change over time: Development of an algorithm for the
732 analyses of longitudinal quantitative MRI measures. *Neuroimage Clin,* 21**,** 101623.
733 KOTTER, M. R., LI, W. W., ZHAO, C. & FRANKLIN, R. J. 2006. Myelin impairs CNS remyelination
734 by inhibiting oligodendrocyte precursor cell differentiation. *J Neurosci,* 26**,** 328-32.
735 KUCHAROVA, K., CHANG, Y., BOOR, A., YONG, V. W. & STALLCUP, W. B. 2011. Reduced
736 inflammation accompanies diminished myelin damage and repair in the NG2 null mouse
737 spinal cord. *J Neuroinflammation,* 8**,** 158.
738 KUCHAROVA, K. & STALLCUP, W. B. 2015. NG2-proteoglycan-dependent contributions of
739 oligodendrocyte progenitors and myeloid cells to myelin damage and repair. *J*
740 *Neuroinflammation,* 12**,** 161.
741 KUHLMANN, T., MIRON, V., CUI, Q., WEGNER, C., ANTEL, J. & BRUCK, W. 2008.
742 Differentiation block of oligodendroglial progenitor cells as a cause for remyelination failure
743 in chronic multiple sclerosis. *Brain,* 131**,** 1749-58.
744 LIN, W., KEMPER, A., DUPREE, J. L., HARDING, H. P., RON, D. & POPKO, B. 2006. Interferon-
745 gamma inhibits central nervous system remyelination through a process modulated by
746 endoplasmic reticulum stress. *Brain,* 129**,** 1306-18.
747 LUBETZKI, C., SOL-FOULON, N. & DESMAZIERES, A. 2020. Nodes of Ranvier during
748 development and repair in the CNS. *Nat Rev Neurol,* 16**,** 426-439.
749 LUCCHINETTI, C., BRUCK, W., PARISI, J., SCHEITHAUER, B., RODRIGUEZ, M. &
750 LASSMANN, H. 1999. A quantitative analysis of oligodendrocytes in multiple sclerosis
751 lesions. A study of 113 cases. *Brain,* 122 (Pt 12)**,** 2279-95.
752 MASON, J. L., TOEWS, A., HOSTETTLER, J. D., MORELL, P., SUZUKI, K., GOLDMAN, J. E. &
753 MATSUSHIMA, G. K. 2004. Oligodendrocytes and progenitors become progressively
754 depleted within chronically demyelinated lesions. *Am J Pathol,* 164**,** 1673-82.
755 MCGINLEY, M. P., GOLDSCHMIDT, C. H. & RAE-GRANT, A. D. 2021. Diagnosis and Treatment
756 of Multiple Sclerosis: A Review. *JAMA,* 325**,** 765-779.
757 MEI, F., FANCY, S. P. J., SHEN, Y. A., NIU, J., ZHAO, C., PRESLEY, B., MIAO, E., LEE, S.,
758 MAYORAL, S. R., REDMOND, S. A., ETXEBERRIA, A., XIAO, L., FRANKLIN, R. J. M.,
759 GREEN, A., HAUSER, S. L. & CHAN, J. R. 2014. Micropillar arrays as a high-throughput
760 screening platform for therapeutics in multiple sclerosis. *Nat Med,* 20**,** 954-960.
761 MELLION, M., EDWARDS, K. R., HUPPERTS, R., DRULOVIC, J., MONTALBAN, X., HARTUNG,
762 H. P., BROCHET, B., CALABRESI, P. A., RUDICK, R., IBRAHIM, A., ZHANG, Y. W., XU,
763 L. & CADAVID, D. 2017. Efficacy Results from the Phase 2b SYNERGY Study: Treatment

764 of Disabling Multiple Sclerosis with the Anti-LINGO-1 Monoclonal Antibody Opicinumab.
765 *Neurology,* 88.
766 MI, S., MILLER, R. H., LEE, X., SCOTT, M. L., SHULAG-MORSKAYA, S., SHAO, Z., CHANG,
767 J., THILL, G., LEVESQUE, M., ZHANG, M., HESSION, C., SAH, D., TRAPP, B., HE, Z.,
768 JUNG, V., MCCOY, J. M. & PEPINSKY, R. B. 2005. LINGO-1 negatively regulates
769 myelination by oligodendrocytes. *Nat Neurosci,* 8**,** 745-51.
770 MOLL, N. M., HONG, E., FAUVEAU, M., NARUSE, M., KERNINON, C., TEPAVCEVIC, V.,
771 KLOPSTEIN, A., SEILHEAN, D., CHEW, L. J., GALLO, V. & OUMESMAR, B. N. 2013.
772 SOX17 is expressed in regenerating oligodendrocytes in experimental models of
773 demyelination and in multiple sclerosis. *Glia*.
774 NEUMANN, B., BAROR, R., ZHAO, C., SEGEL, M., DIETMANN, S., RAWJI, K. S., FOERSTER,
775 S., MCCLAIN, C. R., CHALUT, K., VAN WIJNGAARDEN, P. & FRANKLIN, R. J. M. 2019.
776 Metformin Restores CNS Remyelination Capacity by Rejuvenating Aged Stem Cells. *Cell*
777 *Stem Cell,* 25**,** 473-485 e8.
778 PENDERIS, J., SHIELDS, S. A. & FRANKLIN, R. J. 2003. Impaired remyelination and depletion
779 of oligodendrocyte progenitors does not occur following repeated episodes of focal
780 demyelination in the rat central nervous system. *Brain,* 126**,** 1382-91.
781 PRINEAS, J., RAINE, C. S. & WÍSNIEWSKI, H. 1969. An ultrastructural study of experimental
782 demyelination and remyelination. 3. Chronic experimental allergic encephalomyelitis in the
783 central nervous system. *Lab Invest,* 21**,** 472-83.
784 ROSEN, G. D. & HARRY, J. D. 1990. Brain volume estimation from serial section measurements:
785 a comparison of methodologies. *J Neurosci Methods,* 35**,** 115-24.
786 ROSENBERG, S. S., KELLAND, E. E., TOKAR, E., DE LA TORRE, A. R. & CHAN, J. R. 2008.
787 The geometric and spatial constraints of the microenvironment induce oligodendrocyte
788 differentiation. *Proc Natl Acad Sci U S A,* 105**,** 14662-7.
789 RUSIELEWICZ, T., NAM, J., DAMANAKIS, E., JOHN, G. R., RAINE, C. S. & MELENDEZ-
790 VASQUEZ, C. V. 2014. Accelerated repair of demyelinated CNS lesions in the absence
791 of non-muscle myosin IIB. *Glia,* 62**,** 580-91.
792 SARASWAT, D., SHAYYA, H. J., POLANCO, J. J., TRIPATHI, A., WELLIVER, R. R., POL, S. U.,
793 SEIDMAN, R. A., BROOME, J. E., O'BARA, M. A., VAN KUPPERVELT, T. H., PHILLIPS,
794 J. J., DUTTA, R. & SIM, F. J. 2021a. Overcoming the inhibitory microenvironment
795 surrounding oligodendrocyte progenitor cells following experimental demyelination. *Nat*
796 *Commun,* 12**,** 1923.

797 SARASWAT, D., WELLIVER, R. R., RAVICHANDAR, R., TRIPATHI, A., POLANCO, J. J.,
798 BROOME, J., HURLEY, E., DUTTA, R., FELTRI, M. L. & SIM, F. J. 2021b. Heparanome-
799 Mediated Rescue of Oligodendrocyte Progenitor Quiescence following Inflammatory
800 Demyelination. *J Neurosci,* 41**,** 2245-2263.
801 SARRAZIN, N., CHAVRET-RECULON, E., BACHELIN, C., FELFLI, M., ARAB, R., GILARDEAU,
802 S., BRAZHNIKOVA, E., DUBUS, E., YAHA-CHERIF, L., LORENCEAU, J., PICAUD, S.,
803 ROSOLEN, S., MOISSONNIER, P., POUGET, P. & BARON-VAN EVERCOOREN, A.
804 2022. Failed remyelination of the nonhuman primate optic nerve leads to axon
805 degeneration, retinal damages, and visual dysfunction. *Proc Natl Acad Sci U S A,* 119**,**
806 e2115973119.
807 SERWANSKI, D. R., RASMUSSEN, A. L., BRUNQUELL, C. B., PERKINS, S. S. & NISHIYAMA,
808 A. 2018. Sequential Contribution of Parenchymal and Neural Stem Cell-Derived
809 Oligodendrocyte Precursor Cells toward Remyelination. *Neuroglia,* 1**,** 91-105.
810 SETOGUCHI, T. 2004. Nuclear export of OLIG2 in neural stem cells is essential for ciliary
811 neurotrophic factor-induced astrocyte differentiation. *The Journal of Cell Biology,* 166**,**
812 963-968.
813 SIM, F. J., MCCLAIN, C. R., SCHANZ, S. J., PROTACK, T. L., WINDREM, M. S. & GOLDMAN,
814 S. A. 2011. CD140a identifies a population of highly myelinogenic, migration-competent
815 and efficiently engrafting human oligodendrocyte progenitor cells. *Nat Biotechnol,* 29**,** 934-
816 41.
817 SIM, F. J., ZHAO, C., PENDERIS, J. & FRANKLIN, R. J. 2002. The age-related decrease in CNS
818 remyelination efficiency is attributable to an impairment of both oligodendrocyte progenitor
819 recruitment and differentiation. *J Neurosci,* 22**,** 2451-9.
820 TEPAVCEVIC, V., KERNINON, C., AIGROT, M. S., MEPPIEL, E., MOZAFARI, S., ARNOULD-
821 LAURENT, R., RAVASSARD, P., KENNEDY, T. E., NAIT-OUMESMAR, B. & LUBETZKI,
822 C. 2014. Early netrin-1 expression impairs central nervous system remyelination. *Ann*
823 *Neurol,* 76**,** 252-68.
824 ULRICH, R., SEELIGER, F., KREUTZER, M., GERMANN, P. G. & BAUMGARTNER, W. 2008.
825 Limited remyelination in Theiler's murine encephalomyelitis due to insufficient
826 oligodendroglial differentiation of nerve/glial antigen 2 (NG2)-positive putative
827 oligodendroglial progenitor cells. *Neuropathol Appl Neurobiol,* 34**,** 603-20.
828 WANG, J., SARASWAT, D., SINHA, A. K., POLANCO, J., DIETZ, K., O'BARA, M. A., POL, S. U.,
829 SHAYYA, H. J. & SIM, F. J. 2018. Paired Related Homeobox Protein 1 Regulates
830 Quiescence in Human Oligodendrocyte Progenitors. *Cell Rep,* 25**,** 3435-3450 e6.

831 WAXMAN, S. G., KOCSIS, J. D. & NITTA, K. C. 1979. Lysophosphatidyl choline-induced focal
832 demyelination in the rabbit corpus callosum. Light-microscopic observations. *J Neurol Sci,*
833 44**,** 45-53.
834 WILLIAMS, R. M., LEES, M. B., CAMBI, F. & MACKLIN, W. B. 1982. Chronic Experimental
835 Allergic Encephalomyelitis Induced in Rabbits with Bovine White Matter Proteolipid
836 Apoprotein. *Journal of Neuropathology & Experimental Neurology,* 41**,** 508-521.
837 WINDREM, M. S., NUNES, M. C., RASHBAUM, W. K., SCHWARTZ, T. H., GOODMAN, R. A.,
838 MCKHANN, G., 2ND, ROY, N. S. & GOLDMAN, S. A. 2004. Fetal and adult human
839 oligodendrocyte progenitor cell isolates myelinate the congenitally dysmyelinated brain.
840 *Nat Med,* 10**,** 93-7.
841 WINDREM, M. S., SCHANZ, S. J., GUO, M., TIAN, G. F., WASHCO, V., STANWOOD, N.,
842 RASBAND, M., ROY, N. S., NEDERGAARD, M., HAVTON, L. A., WANG, S. &
843 GOLDMAN, S. A. 2008. Neonatal chimerization with human glial progenitor cells can both
844 remyelinate and rescue the otherwise lethally hypomyelinated shiverer mouse. *Cell Stem*
845 *Cell,* 2**,** 553-65.
846 WINDREM, M. S., SCHANZ, S. J., MORROW, C., MUNIR, J., CHANDLER-MILITELLO, D.,
847 WANG, S. & GOLDMAN, S. A. 2014. A competitive advantage by neonatally engrafted
848 human glial progenitors yields mice whose brains are chimeric for human glia. *J Neurosci,*
849 34**,** 16153-61.
850 WOLSWIJK, G. 1998. Chronic stage multiple sclerosis lesions contain a relatively quiescent
851 population of oligodendrocyte precursor cells. *J Neurosci,* 18**,** 601-9.
852 WOODRUFF, R. H., FRUTTIGER, M., RICHARDSON, W. D. & FRANKLIN, R. J. 2004. Platelet-
853 derived growth factor regulates oligodendrocyte progenitor numbers in adult CNS and
854 their response following CNS demyelination. *Mol Cell Neurosci,* 25**,** 252-62.
855 XING, Y. L., CHUANG, B. H. A., POH, J., MORADI, K., MITEW, S., KILPATRICK, T. J., OSANAI,
856 Y. & MERSON, T. D. 2021. A Novel Pharmacogenetic Model for Highly Efficient Ablation
857 of Oligodendrocyte Progenitor Cells in the Adult Mouse CNS. *bioRxiv***,**
858 2021.05.13.443012.
859 YEUNG, M. S. Y., DJELLOUL, M., STEINER, E., BERNARD, S., SALEHPOUR, M., POSSNERT,
860 G., BRUNDIN, L. & FRISEN, J. 2019. Publisher Correction: Dynamics of oligodendrocyte
861 generation in multiple sclerosis. *Nature,* 566**,** E9.
862 ZAWADZKA, M., RIVERS, L. E., FANCY, S. P., ZHAO, C., TRIPATHI, R., JAMEN, F., YOUNG,
863 K., GONCHAREVICH, A., POHL, H., RIZZI, M., ROWITCH, D. H., KESSARIS, N.,
864 SUTER, U., RICHARDSON, W. D. & FRANKLIN, R. J. 2010. CNS-resident glial

865 progenitor/stem cells produce Schwann cells as well as oligodendrocytes during repair of
866 CNS demyelination. *Cell Stem Cell,* 6**,** 578-90.
867 ZHAO, C., MA, D., ZAWADZKA, M., FANCY, S. P., ELIS-WILLIAMS, L., BOUVIER, G.,
868 STOCKLEY, J. H., DE CASTRO, G. M., WANG, B., JACOBS, S., CASACCIA, P. &
869 FRANKLIN, R. J. 2015. Sox2 Sustains Recruitment of Oligodendrocyte Progenitor Cells
870 following CNS Demyelination and Primes Them for Differentiation during Remyelination.
871 *J Neurosci,* 35**,** 11482-99.

872

873

874 **TABLES**

Table 1. Animal and lesion numbers per timepoint.

Timepoint (dpl)	Large Lesions		Small Lesions	
	Animals	Lesions	Animals	Lesions
7	6	9	4	6
14	5	8	4	4
21	4	8	4	4
56	5	7		
180	3	4		

875

876 **FIGURE LEGENDS**

877 **Figure 1. Large regions of demyelination following injection of lysolecithin into rabbit**
878 **subcortical white matter persisted for at least 180 days. A**, Scale diagram representing
879 injection sites and white matter tract size (mouse included for reference). **B**, Lysolecithin-induced
880 lesion at 14 days post-lesion (dpl) in the rabbit stained for FluoroMyelin (FM, red) and 4',6'-
881 diamidino-2-phenylindole (DAPI, blue). White dotted line indicates lesion border. **C-D**, Lesion
882 volume (**C**) and maximal cross-sectional area (**D**) of lesions overtime. **E**, lesion reconstruction
883 using FM and DAPI sampled every 1.6 mm, demonstrating typical lesion geometry at 7 dpl. Each
884 point represents a single lesion. Mean ± SEM shown. Scale: 5 mm (**A**), 500 μm (**B**), 300 μm (**E**).

885

886 **Figure 2. Insufficient oligodendrocyte progenitor cell repopulation and oligodendrocyte**
887 **generation following demyelination in rabbit white matter. A**, Oligodendrocyte progenitor
888 cells (OPCs) and oligodendrocytes (OLs) were identified as $Olig2^{+}CC1^{-}$ and $Olig2^{+}CC1^{+}$,
889 respectively. Insert shows a high magnification image of a $CC1^{+}$ (green) OL. The density of each
890 cell type was quantified at each time point (**B-E**). **B**, Density of $Olig2^{+}$ oligodendrocyte lineage
891 cells. **C**, Density of $CC1^{-}Olig2^{+}$ defined OPCs cells. **D,** Density of $CC1^{+}Olig2^{+}$ defined OLs. **E**, The
892 percentage of $CC1^{+}$ oligodendrocytes among total $Olig2^{+}$ OL lineage cells. Mean ± SEM shown.
893 Dashed line on each graph represents the mean of normal white matter (left bar, n = 6). Following
894 one-way ANOVA, pairwise comparisons to normal were performed (Tukey's multiple comparisons
895 post-test). *, **, ***, and **** indicate $p \leq 0.05$, 0.01, 0.001, and 0.0001, respectively. Scale: 50 μm
896 (**A**), 10 μm (**A**, insert).

897

898 **Figure 3. Abundant oligodendrocyte progenitor cell activation but low proliferation**
899 **following injury. A-D**, Representative images of normal white matter (**A**), or lesion at 14 days
900 post-lesion (dpl) (**B**), 56 dpl (**C**), 180 dpl (**D**). Activated Sox2$^+$ OPCs (cyan), proliferative Ki67$^+$
901 OPCs (green) were identified by colocalization with Olig2 (red). Insert shows high magnification
902 of labelled cells. Individual Sox2$^+$Olig2$^+$ cells are indicated with arrows in **C** and **D**. **E**, Density of
903 activated Sox2$^+$ OPCs following demyelination. **F**, Proportion of Ki67$^+$ proliferating Olig2$^+$ cells. **G**,
904 Proportion of Ki67$^+$ proliferating cells among Sox2$^+$Olig2$^+$ activated OPCs. **H**, An example of Sox2
905 (cyan)-expressing Gfap$^+$ (green) astrocyte within the demyelinating lesion. **I**, Quantification of
906 Sox2$^+$Olig2$^-$ astrocytic cell density. Mean ± SEM shown. Dashed lines on graph represent mean
907 of normal white matter (left bar, n =6). One-way ANOVA was performed across time points and
908 specific pairwise comparisons are shown, between normal and peak, peak and 180 dpl, and
909 normal and 180 dpl (other pairwise comparisons excluded for clarity) (Tukey's multiple
910 comparisons post-test). *, **, ***, and **** indicate $p \leq 0.05$, 0.01, 0.001, and 0.0001, respectively.
911 Scale: 200 µm (**A-D**), 10 µm (**A**, inserts), 5 µm (**H**).
912
913 **Figure 4. Large lesions displayed abundant gliosis, with the microglia/macrophage**
914 **response greatest at early timepoints. A-D**, Iba1 (red) and Gfap (green) were used as markers
915 of microglia/macrophages and astrocytes, respectively, with nuclei labeled with DAPI (blue).
916 Lesion borders (dashed line). Inserts show higher power confocal images of boxed areas. **E**, Iba1
917 mean fluorescent intensity (MFI). The intensity of staining in the distant corpus callosum was
918 considered normal appearing white matter (NAWM) for quantitative comparisons and to control
919 for batch and animal staining variability. **F**, Total Gfap$^+$ area above threshold was quantified and
920 shown as a percentage of total lesion area. **G**, DAPI$^+$ cell density within the lesion (cells / mm^2).
921 Mean ± SEM shown. Dashed lines on graph represent mean of distant normal appearing white
922 matter (NAWM) (n= 29) or normal uninjured animals (n=3). Following one-way ANOVA, pairwise
923 comparisons to NAWM were performed (Tukey's multiple comparisons post-test). *, **, ***, and
924 **** indicate $p \leq 0.05$, 0.01, 0.001, and 0.0001, respectively. Scale: 500 µm (**A-D**), 25 µm (**A**,
925 inserts).
926
927 **Figure 5. Myelin ladened microglia/macrophages were abundant within the lesion center**
928 **of large rabbit lesions. A-B**, Low power imaging revealed Iba1$^+$ (red) vesicular structures filling
929 the lesion core at 14 (**A**) and 56 dpl (**B**). **C-E**, Confocal microscopy with DAPI (blue)(**C**), myelin
930 basic protein (Mbp, gray) (**D**, same field), and neurofilament (NF, green) (**E**) co-staining with Iba1
931 (red). The majority of vesicular structures surrounded by Iba1$^+$ immunoreactivity contained myelin

932 debris at 14 dpl while a small minority contained neurofilament. At 56 dpl, a substantial proportion
933 of vesicular structures did not contain immunoreactivity to Mbp or NF. Scale: 100 μm (**A-B**), 20
934 μm (**C-E**).
935
936 **Figure 6. The perilesion white matter displayed hypercellularity and disturbed myelin**
937 **structure. A**, Evolution of lysolecithin-induced lesions in the rabbit over time stained for
938 FluoroMyelin (FM, red) and DAPI (blue/cyan). White dashed line indicates lesion bounds. An area
939 of hypercellularity extending past the lesion boundary was noted (blue dashed line), referred to
940 as the perilesion white matter (PLWM). **A'**, Higher magnification images of the outlined areas
941 (white rectangles) depicting the observed cellularity changes between lesion, PLWM, and more
942 distant normal appearing white matter (NAWM). **B**, Quantification of observed changes in
943 cellularity between the different regions at 21 dpl (n = 6-22, one-way ANOVA, $F(3,38) = 147.3$, p
944 $= 0.0001$). Mean ± SEM shown. Dashed lines on graph represent mean of normal white matter.
945 Following one-way ANOVA, pairwise comparisons to NAWM were performed (Tukey's multiple
946 comparisons post-test). *, **, ***, and **** indicate $p \leq 0.05$, 0.01, 0.001, and 0.0001, respectively.
947 **C**, Comparison of mean maximal cross-sectional area of lesion and PLWM areas. **D-E**,
948 Representative confocal images of NAWM stained for myelin (Mbp, gray), and axonal markers
949 (NF, green; App, red). **F-G**, Following demyelination at 7 to 56 dpl, lesions were imaged by
950 widefield epifluorescence (left panels). **F'-G'**, Higher power confocal images within the lesion
951 (right panels). Myelin loss was evident in the lesion following injection of lysolecithin and persisted
952 thereafter. Myelin debris was present in the lesion core at all timepoints. Axonal loss was localized
953 to the central portion of the lesion and corresponded to increased App (red) staining at 7 dpl.
954 Scale: 500 μm (**A, F-G**), 100 μm (**A'**), 25 μm (**D-E, F'-G'**).
955
956 **Figure 7. Oligodendrocyte density was reduced in the perilesion white matter, with**
957 **increased expression of Prrx1 among OPCs at the lesion edge. A-E**, Three regions were
958 defined for regional analysis: perilesion white matter (PLWM) (light green dashed line), lesion
959 edge (green dashed line), and lesion core (dark green dashed line). PLWM was defined as an
960 area of mild hypercellularity and extended past the lesion border. The lesion proper was divided
961 into the edge and core regions, with the edge defined as the outermost 75μm rim. Cross-sectional
962 columns of a 56 dpl lesion covering the various regions stained for DAPI (**A**), OLs ($Olig2^+CC1^+$)
963 (**B**), active oligodendrocyte progenitor cell ($Olig2^+Sox2^+$) (**C**), proliferative OPCs ($Olig2^+Ki67^+$) (**D**),
964 and $Gfap^+$ astrocytes (**E**). **F-H**, Quantification of cell density and/or proportion of total
965 oligodendrocyte linage cells between regions for OLs ($Olig2^+CC1^+$, **F**), OPCs ($Olig2^+CC1^-$, **G**), and

966 activated OPCs (Olig2$^+$Sox2$^+$, **H**). Mean ± SEM shown. Horizontal bands represent mean ± 1x
967 SEM of the normal white matter for each measurement (n = 3 rabbits). Two-way ANOVA was
968 performed across time (TME: time main effect) and regions (RME: regional main effect). *, **, ***,
969 and **** indicate p ≤ 0.05, 0.01, 0.001, and 0.0001, respectively. Individual pairwise comparisons
970 not shown. **I-J**, a combination of *in situ* hybridization and immunohistochemistry was used to label
971 Prrx1 mRNA (gray) and Olig2 protein (red). Arrowheads indicate coexpression of Olig2 and Prrx1.
972 **K-L**, Density (**K**), and percentage (**L**) of Prrx1$^+$Olig2$^+$ cells in the lesion edge. Mean ± SEM shown
973 (n=3). * and *** indicate t-test p ≤ 0.05 and 0.001, respectively. **M**, an example of a cytoplasmic
974 Olig2 immunoreactive cell at 56 dpl. These cells were observed in most lesion sections following
975 demyelination (~1-2 cells per section, most commonly at 56 dpl). Scale: 200 µm (**A-E**), 10 µm
976 (**M**).
977
978 **Figure 8. Small rabbit lesions displayed a reduced microglial response.** Small (0.35 µL) (**A-**
979 **C**) and large (5 µL) (**D-F**) volume lesions were created via stereotaxic injection of lysolecithin, and
980 stained for DAPI (blue), Gfap (green), and Iba1(red). White dashed lines indicate lesion border.
981 **G**, Lesion volume calculated by serial section reconstruction of each lesion. **H**, Lesion cell density
982 (DAPI$^+$/mm^2). **I**, Quantification of astrocyte response. Total Gfap$^+$ area above threshold was
983 quantified and shown as a percentage of total lesion area. **J**, microglial response was quantified
984 by mean fluorescent intensity (MFI). Mean ± SEM shown. Dashed lines on graph represent mean
985 of distant normal appearing white matter (n= 29). 0.35 µL injections of lysolecithin produced
986 lesions with significantly smaller volumes as compared to 5 µL at every time point (n= 4-9, two-
987 way ANOVA, volume factor $F(1,33) = 72.5$, $p < 0.0001$). Small and large volume lesions displayed
988 similar levels of hypercellularity (volume factor $F(1,21) = 3.37$, $p > 0.05$), and similar astrocyte
989 responses (n= 4-9, two-way ANOVA, volume factor $F(1,32) = 0.05$, $p > 0.05$). However, Iba1 MFI
990 was significantly greater in large volume lesions compared to small lesions (n= 4-9, two-way
991 ANOVA, volume factor $F(1,28) = 17.39$, $p = 0.0003$). Pairwise comparisons of small vs. large
992 lesions at each time point shown for lesion volume (**G**) and microglial response (**J**) (Sidak's
993 multiple comparisons post-test). *, **, ***, and **** indicate p ≤ 0.05, 0.01, 0.001, and 0.0001,
994 respectively. Scale: 200 µm.
995
996 **Figure 9. Small volume lesions displayed less oligodendrocyte progenitor cell activation**
997 **and dramatically reduced proliferation. A-C**, Activated Sox2$^+$ oligodendrocyte progenitor cells
998 (OPCs) (**B**, cyan), and proliferative Ki67$^+$ OPCs (**C**, green) were identified by colocalization with
999 Olig2 at 14 dpl in small and large volume lesions. Insert shows higher magnification of labelled

1000 cells. **D**, Oligodendrocyte (OL) differentiation was assessed by CC1 (green) and Olig2 (red)
1001 immunofluorescence. A representative $CC1^+Olig2^+$ cell is shown (**D**, inset). In large lesions, the
1002 quantification of cell density was performed in the lesion edge. **E-K**, Quantification of $Olig2^+$ OL
1003 lineage cell density (cells/mm^2, **E**), the density of $Sox2^+Olig2^+$ activated OPCs (cell/mm^2, **F**), the
1004 percentage of Ki67-defined proliferating $Olig2^+$ cells (**G**), the percentage of Ki67-defined
1005 proliferating $Sox2^+Olig2^+$ OPCs (**H**), density of $CC1^-Olig2^+$ cells (cells/mm^2, **I**), density of
1006 $CC1^+Olig2^+$ oligodendrocytes (cells/mm^2, **J**), and the percentage of $CC1^+Olig2^+$ oligodendrocytes
1007 among the $Olig2^+$ population (**K**) in small and large lesions. Mean ± SEM shown. Dashed lines on
1008 each graph represent mean of normal uninjured white matter (n = 3 rabbits). **E-K**, Two-way
1009 ANOVA revealed a significant effects of lesion volume on activated (**F**) and proliferating (**G-H**)
1010 OPC densities ($p < 0.05$). The other endpoints were not significantly altered by lesion volume. **F-**
1011 **H**, Pairwise comparisons of small vs. large lesions at each time point were performed and shown
1012 where significant (Sidak multiple comparisons post-test). *, **, ***, and **** indicate $p \leq 0.05$, 0.01,
1013 0.001, and 0.0001, respectively. Scale: 50 µm (**A-D**), 10 µm (**B-D**, insets).
1014
1015 **Supplemental Figure 1. Markers of the innate immune response were increased in the**
1016 **perilesion white matter adjacent to demyelination.** The white matter directly adjacent to the
1017 lesion area, termed the perilesion white matter (PLWM), and defined by increased cellularity
1018 compared to normal white matter exhibited increased staining for markers of microglia and
1019 astrocytes following demyelination. White dashed line indicates lesion bounds, and the PLWM
1020 was identified as an area of DAPI hypercellularity (**A**, blue) extending past the lesion boundary
1021 (blue dashed line). Iba1 was used to identify microglia (**B**, red) and astrocytes identified using
1022 Gfap (**C**, green). **D-E,** Quantification of Iba1 mean fluorescence intensity (MFI) (**D**), and Gfap %
1023 area (**E**). Mean ± SEM shown. Dashed lines on each graph represent mean of normal appearing
1024 white matter (NAWM). One-way ANOVA revealed a significant effect of time on both Iba1 and
1025 Gfap. Pairwise comparisons to NAWM were performed at each dpl (Tukey's multiple comparisons
1026 post-test). *, and **** indicate $p \leq 0.05$, and 0.0001, respectively. Scale, 250 µm.
1027
1028 **Supplemental Figure 2. Axon deficient center was dependent on lysolecithin injection**
1029 **volume.** Axonal density following demyelination was assessed by neurofilament
1030 immunofluorescence (green) as a function of volume of lysolecithin injected and days post lesion
1031 (dpl). DAPI (blue) hypercellularity was used to define the lesion border (outer white line).
1032 Neurofilament-expressing axonal fibers were observed throughout the lesion following injection
1033 of 0.35 µL (**A**) at 7 days post-lesion (dpl). With injections of 1 µL (**B**) and 5 µL (**C**), a central region

of axonal loss was observed at 7 dpl (orange lines). The area of central axonal loss increased with injection volume. **C-F**, the central area of axonal loss persisted until 56 dpl. The area of the central region of axonal loss (orange line) compared to the total lesion area (grey line) (**G**). The size of the central region of axonal loss remained stable with time, while the overall lesion area reduced. **H**, Axonal density in the lesion edge was compared to the lesion core (which contained the central region of axonal loss). Quantitative estimation of axonal density following 5 µL lysolecithin injection was performed using a thresholding approach. Mean ± SEM shown. Dashed lines on each graph represent mean of normal appearing white matter (NAWM). Two-way ANOVA showed a significantly greater axonal density in the lesion edge than core ($n = 8\text{-}14$, region main effect $p < 0.0001$) and indicated a time dependent effect on axonal density (time main effect $p = 0.014$). Pairwise comparisons of 14, 21 and 56 dpl with 7 dpl identified a significant decrease in axonal density at 21 and 56 dpl in the lesion core only (* indicates Sidak $p \leq 0.05$). **I,** the axonal density in small lesions was directly compared to the axonal density in large lesion edge at 7 dpl. Mean ± SEM shown. There was no significant difference (t-test $p > 0.05$). Scale, 200 µm.

Supplemental Figure 3. Summary of oligodendroglia population dynamics in small and large lesions, compared to mouse. Meta-analysis of rabbit large and small lesions alongside equivalently sized mouse spinal cord lesions. Comparative mouse data obtained from previously published quantification of oligodendrocyte progenitor cell (OPC)/NG2 density (Garay et al., 2011, Kucharova and Stallcup, 2015), oligodendrocyte (OL)/Plp1 (Fancy et al., 2009), $Sox2^+Olig2^+$ OPCs and $Ki67^+Olig2^+$ OPCs (Zhao et al., 2015 and unpublished data). **A**, Table summarizing the effects of species and lesion volume on various cellular parameters following demyelination. The time of peak density in days post lesion (dpl) as well as the density relative to normal uninjured white matter are presented for OPC repopulation, OL repopulation, activated OPC density ($Sox2^+$), and proliferating OPC density ($Ki67^+$). ↑ and ↑↑ indicate significant increases in density relative to uninjured normal white matter. ns = non-significant from normal white matter density. **B**, Scale diagrams comparing large and small rabbit lesions and mouse spinal cord lesions. **C**, Profiles of overall OPC density and the relative density of $Sox2^+$ activated and $Ki67^+$ proliferating OPCs. Scale, 2 mm.

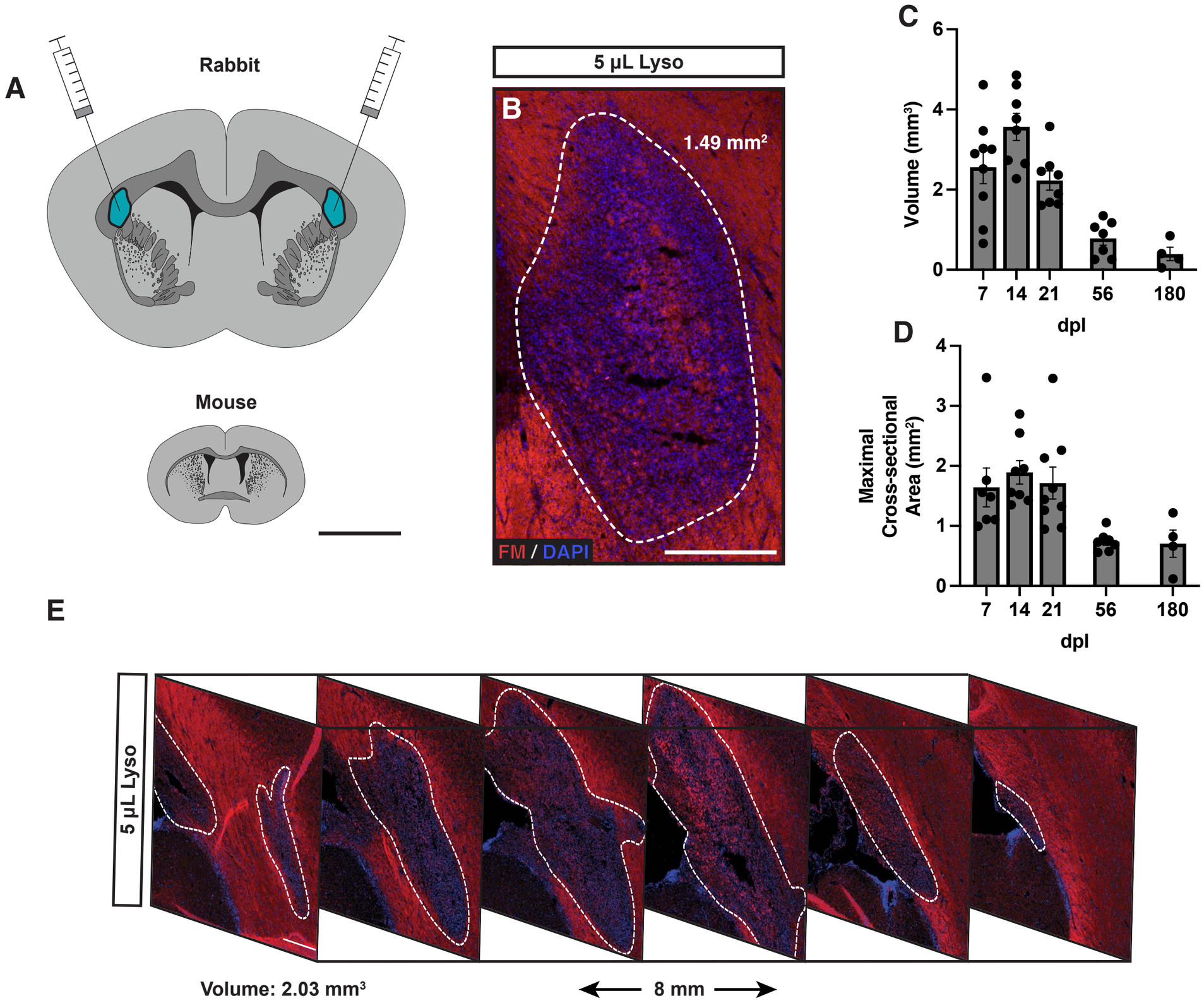
A
Rabbit
Mouse
5 µL Lyso
B
1.49 mm²
FM / DAPI
C
Volume (mm³)
dpl
7
14
21
56
180
D
Maximal Cross-sectional Area (mm²)
dpl
E
5 µL Lyso
Volume: 2.03 mm³
8 mm

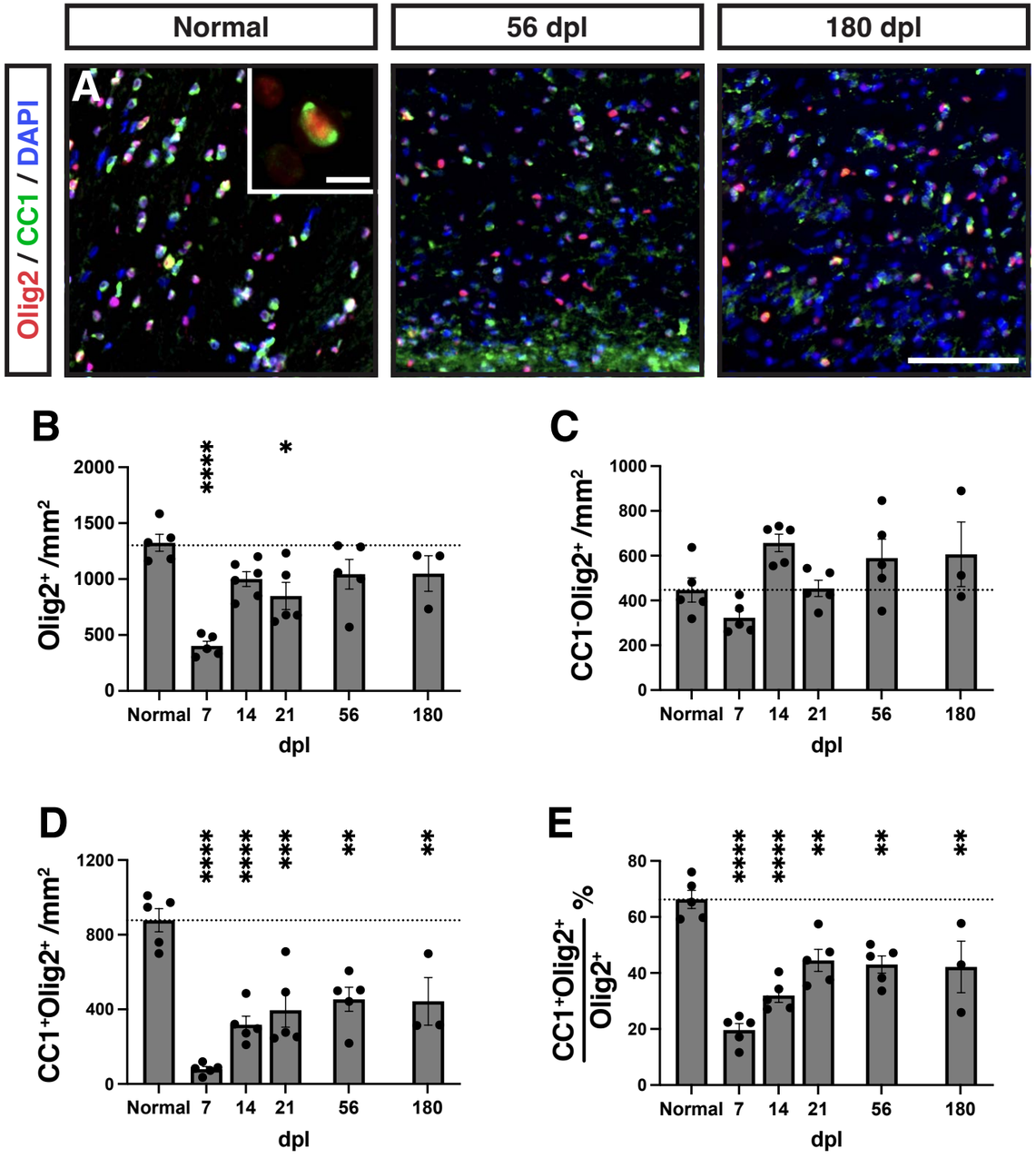
Normal
56 dpl
180 dpl
Olig2 / CC1 / DAPI
A
B
Olig2+ /mm2
2000
1500
1000
500
0
****
*
Normal 7 14 21 56 180
dpl
C
CC1-Olig2+ /mm2
1000
800
600
400
200
0
Normal 7 14 21 56 180
dpl
D
CC1+Olig2+ /mm2
1200
800
400
0
****
****
***
**
**
Normal 7 14 21 56 180
dpl
E
CC1+Olig2+ / Olig2+ %
80
60
40
20
0
****
****
**
**
**
Normal 7 14 21 56 180
dpl

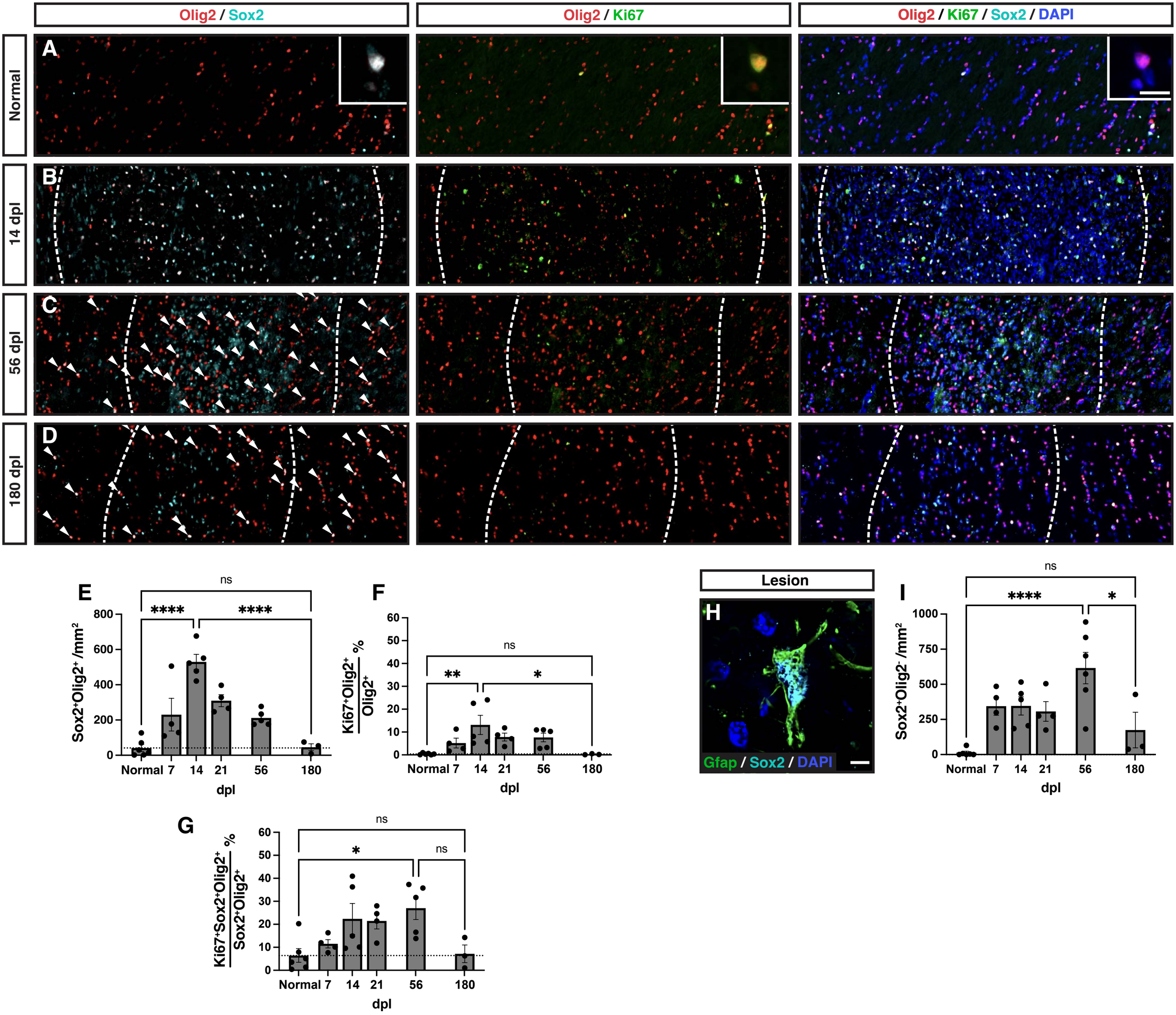
Olig2 / Sox2
Olig2 / Ki67
Olig2 / Ki67 / Sox2 / DAPI
Normal
14 dpl
56 dpl
180 dpl
A
B
C
D
E
F
G
H
I
Lesion
Gfap / Sox2 / DAPI
Sox2+Olig2+ /mm2
Ki67+Olig2+ % / Olig2+
Ki67+Sox2+Olig2+ % / Sox2+Olig2+
Sox2+Olig2- /mm2
Normal 7 14 21 56 180
dpl
ns
****
**
*

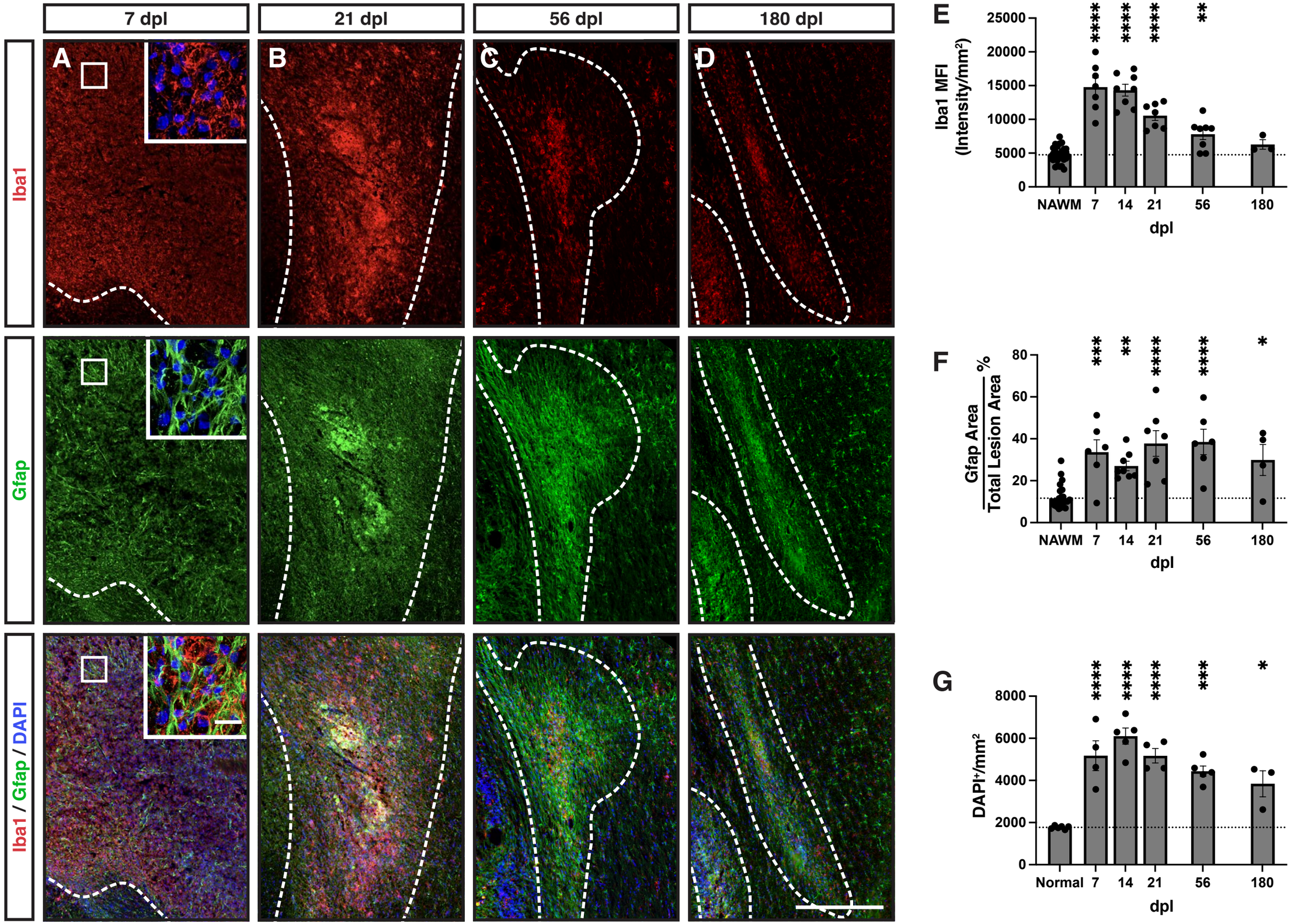
7 dpl
21 dpl
56 dpl
180 dpl
A
B
C
D
Iba1
Gfap
Iba1 / Gfap / DAPI
E
Iba1 MFI (Intensity/mm²)
25000
20000
15000
10000
5000
0
NAWM
7
14
21
56
180
dpl
F
Gfap Area / Total Lesion Area %
80
60
40
20
0
NAWM
7
14
21
56
180
dpl
G
DAPI⁺/mm²
8000
6000
4000
2000
0
Normal
7
14
21
56
180
dpl

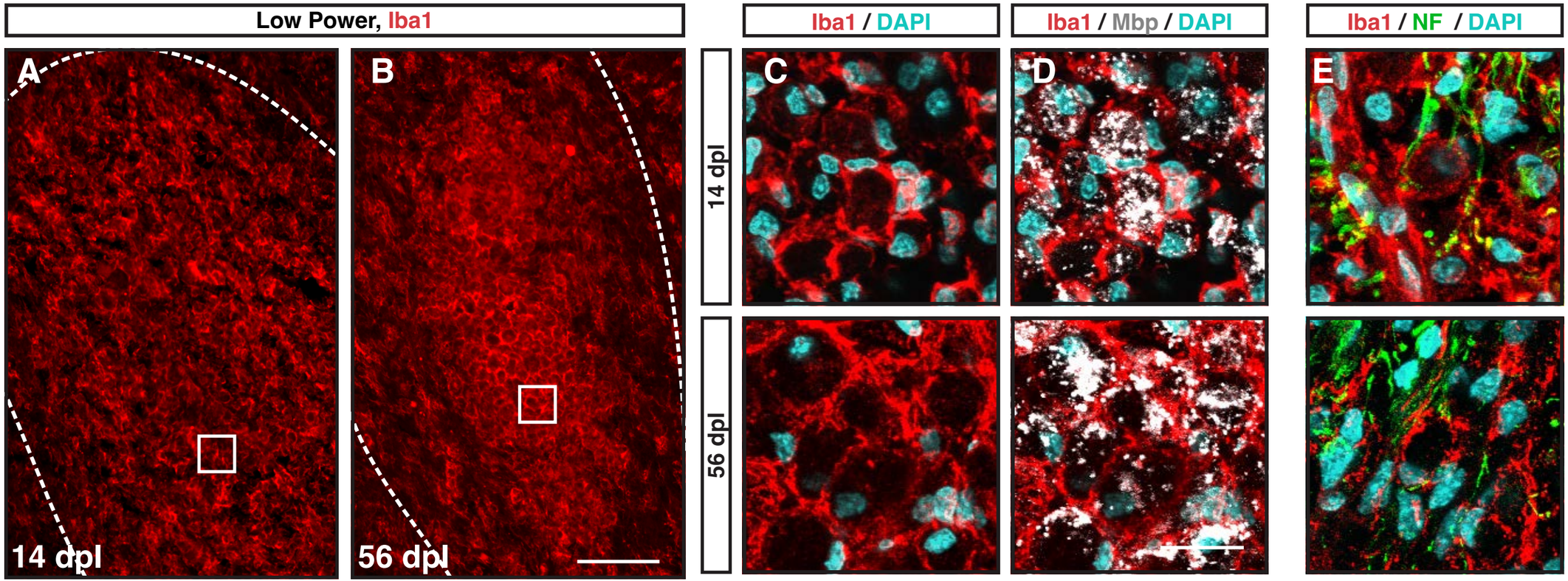
Low Power, Iba1
Iba1 / DAPI
Iba1 / Mbp / DAPI
Iba1 / NF / DAPI
A
B
C
D
E
14 dpl
56 dpl
14 dpl
56 dpl

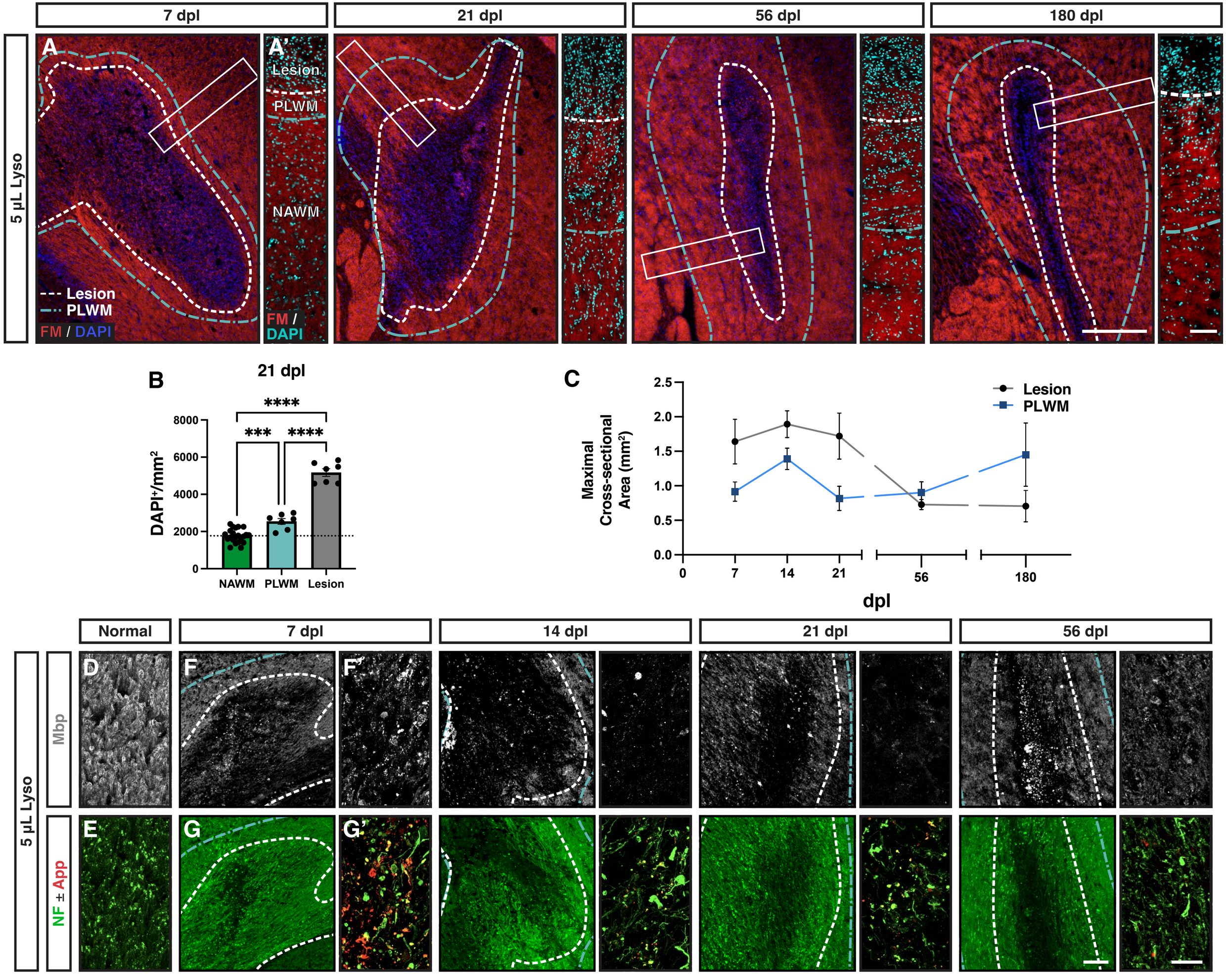
7 dpl
21 dpl
56 dpl
180 dpl
5 µL Lyso
A
A'
Lesion
PLWM
NAWM
Lesion
PLWM
FM / DAPI
FM / DAPI
B
21 dpl
DAPI+/mm2
8000
6000
4000
2000
0
****
***
****
NAWM
PLWM
Lesion
C
Maximal Cross-sectional Area (mm2)
2.5
2.0
1.5
1.0
0.5
0.0
0
7
14
21
56
180
dpl
Lesion
PLWM
Normal
7 dpl
14 dpl
21 dpl
56 dpl
5 µL Lyso
Mbp
NF ± App
D
E
F
F'
G
G'

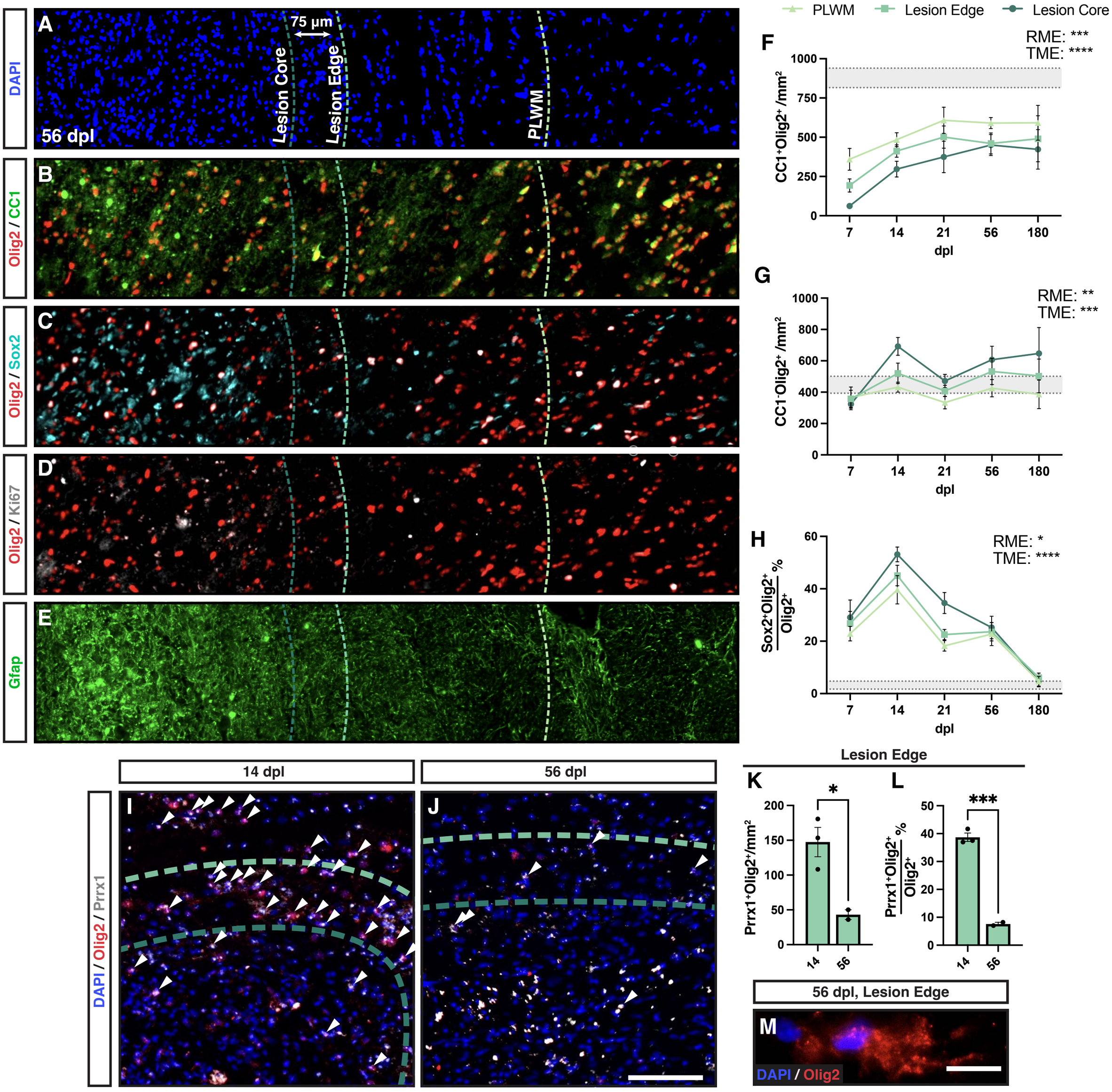
A
DAPI
56 dpl
75 µm
Lesion Core
Lesion Edge
PLWM
B
Olig2 / CC1
C
Olig2 / Sox2
D
Olig2 / Ki67
E
Gfap
PLWM
Lesion Edge
Lesion Core
F
RME: ***
TME: ****
CC1+Olig2+ /mm2
dpl
G
RME: **
TME: ***
CC1-Olig2+ /mm2
dpl
H
RME: *
TME: ****
Sox2+Olig2+ / Olig2+ %
dpl
14 dpl
56 dpl
I
J
DAPI / Olig2 / Prrx1
Lesion Edge
K
Prrx1+Olig2+/mm2
L
Prrx1+Olig2+ / Olig2+ %
56 dpl, Lesion Edge
M
DAPI / Olig2

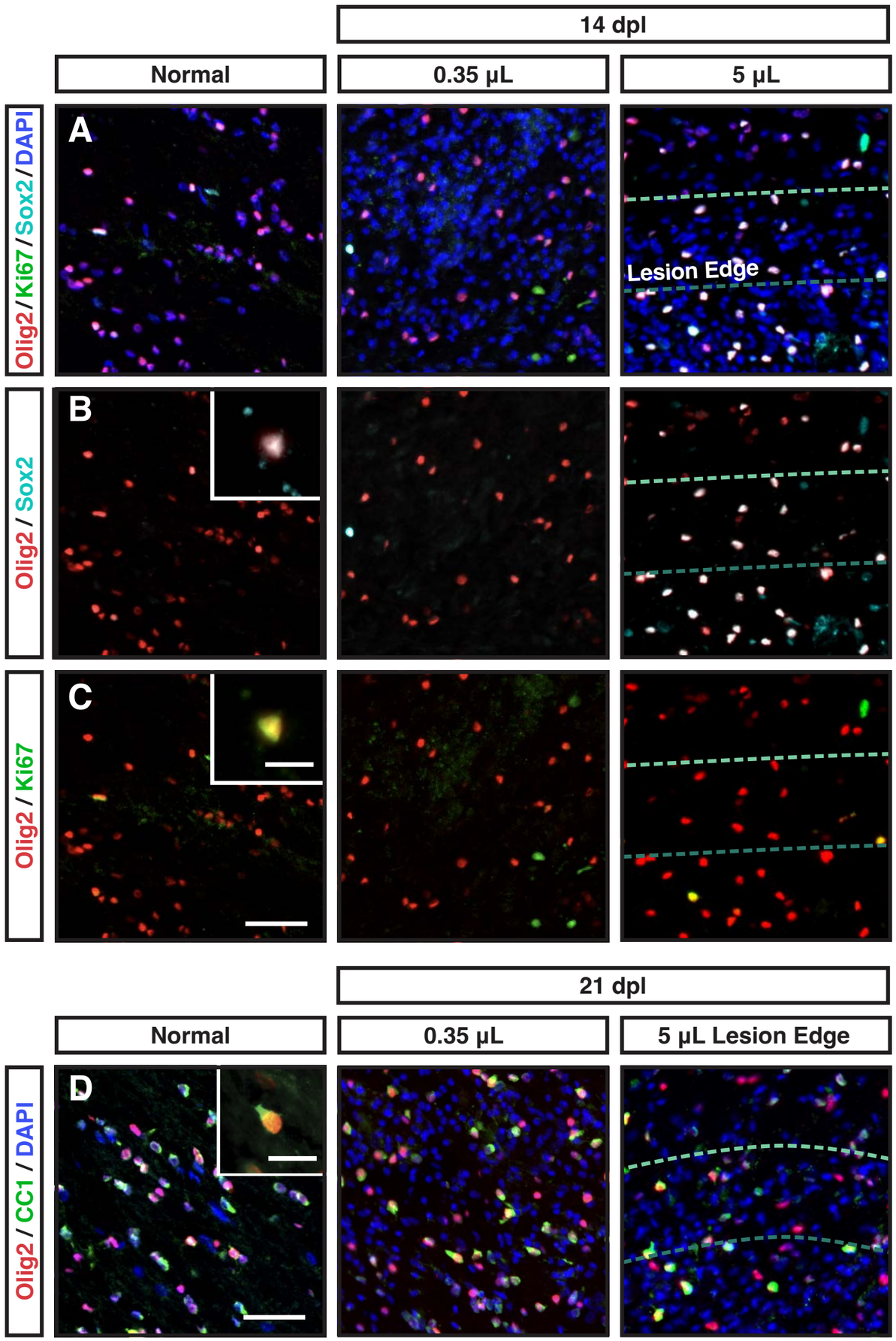
14 dpl
Normal
0.35 µL
5 µL
Olig2/Ki67/Sox2/DAPI
A
Lesion Edge
Olig2 / Sox2
B
Olig2 / Ki67
C
21 dpl
Normal
0.35 µL
5 µL Lesion Edge
Olig2 / CC1 / DAPI
D

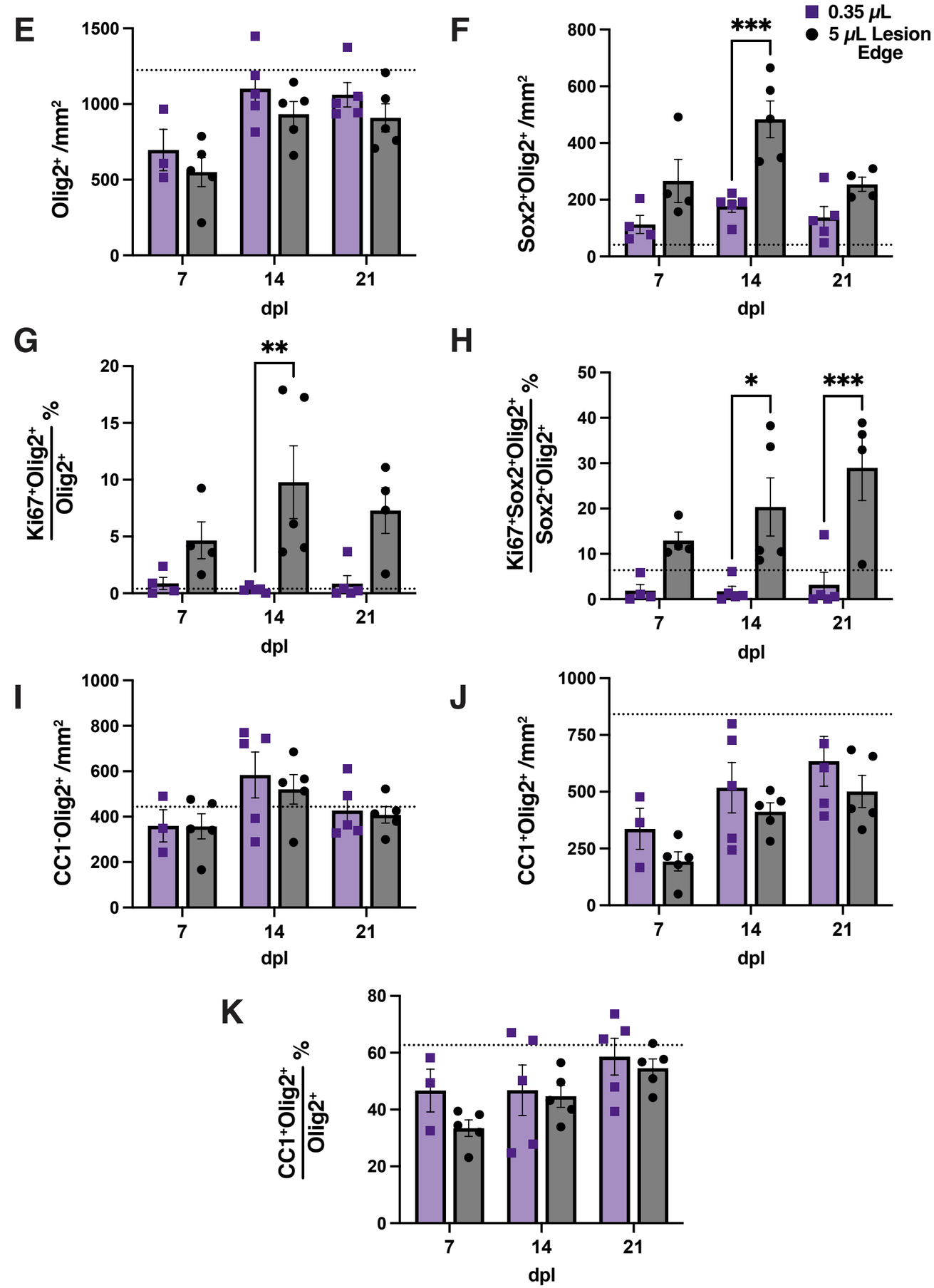
E
Olig2⁺ /mm²
dpl
F
Sox2⁺Olig2⁺ /mm²
0.35 µL
5 µL Lesion Edge
***
G
Ki67⁺Olig2⁺ / Olig2⁺ %
**
H
Ki67⁺Sox2⁺Olig2⁺ / Sox2⁺Olig2⁺ %
*
***
I
CC1⁻Olig2⁺ /mm²
J
CC1⁺Olig2⁺ /mm²
K
CC1⁺Olig2⁺ / Olig2⁺ %

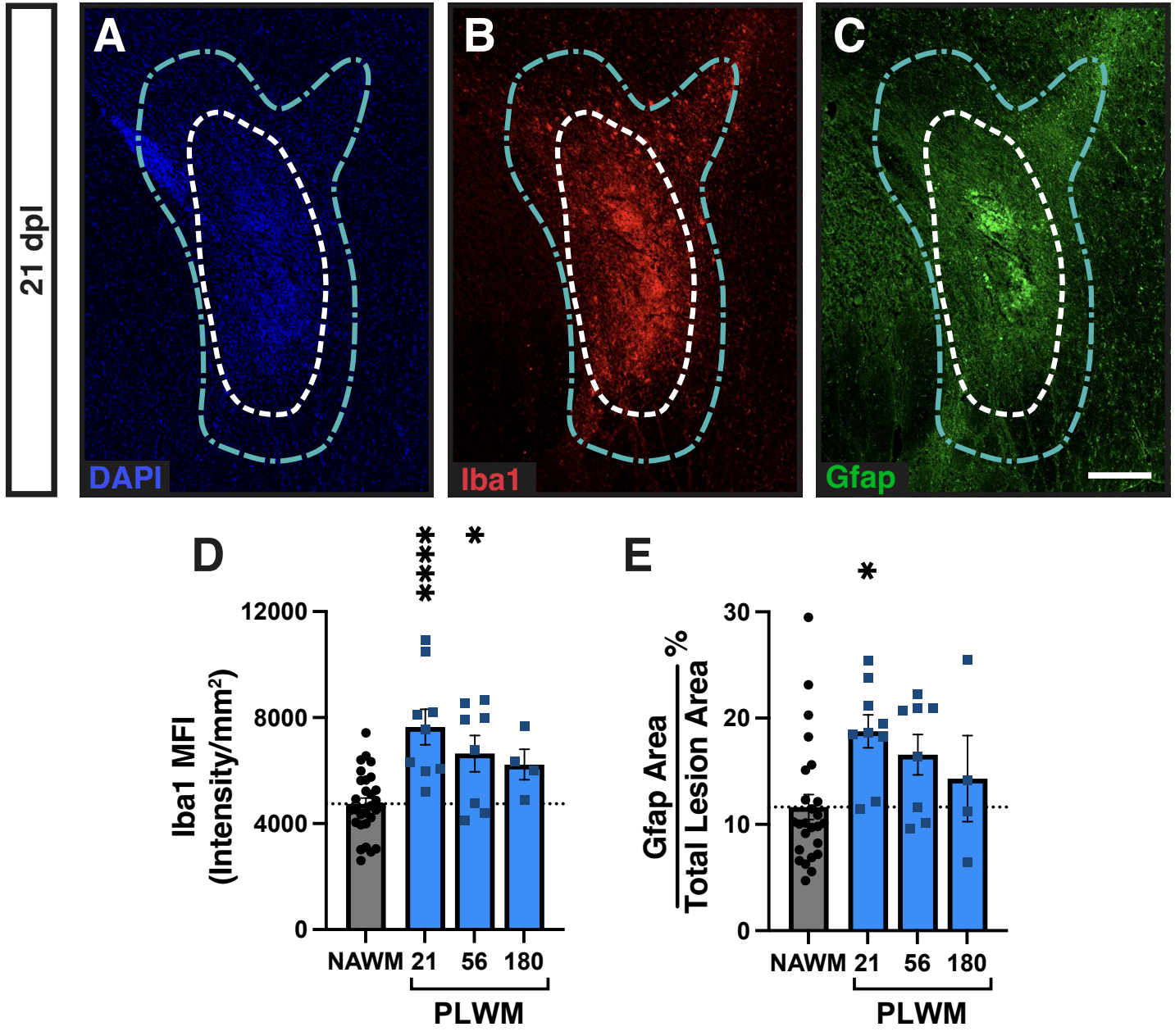
21 dpl
A
DAPI
B
Iba1
C
Gfap
D
****
*
Iba1 MFI
(Intensity/mm²)
12000
8000
4000
0
NAWM
21
56
180
PLWM
E
*
Gfap Area
Total Lesion Area
%
30
20
10
0
NAWM
21
56
180
PLWM

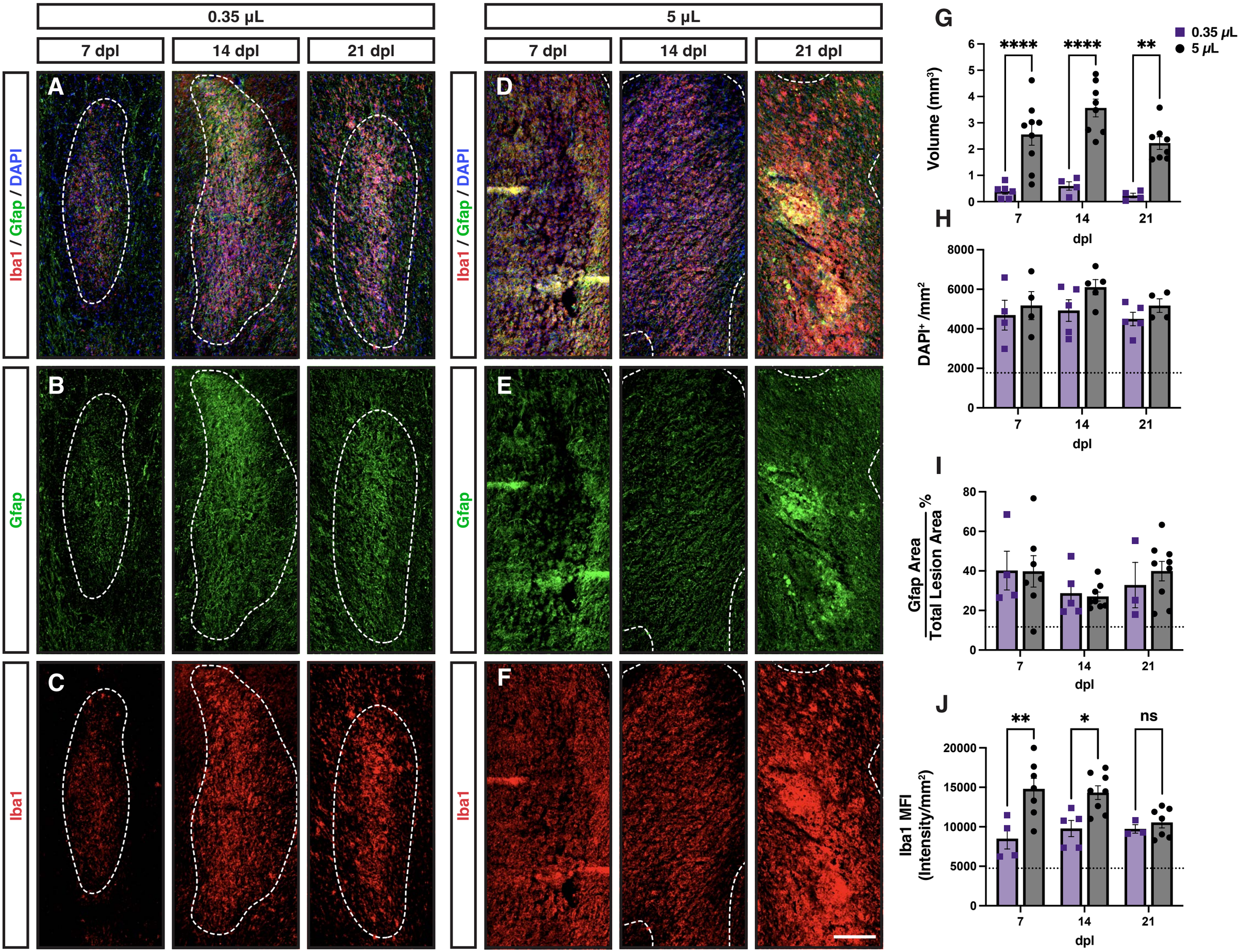
0.35 µL
5 µL
7 dpl
14 dpl
21 dpl
Iba1 / Gfap / DAPI
Gfap
Iba1
A
B
C
D
E
F
G
H
I
J
0.35 µL
5 µL
Volume (mm³)
****
****
**
dpl
DAPI⁺ /mm²
Gfap Area / Total Lesion Area %
Iba1 MFI (Intensity/mm²)
**
*
ns

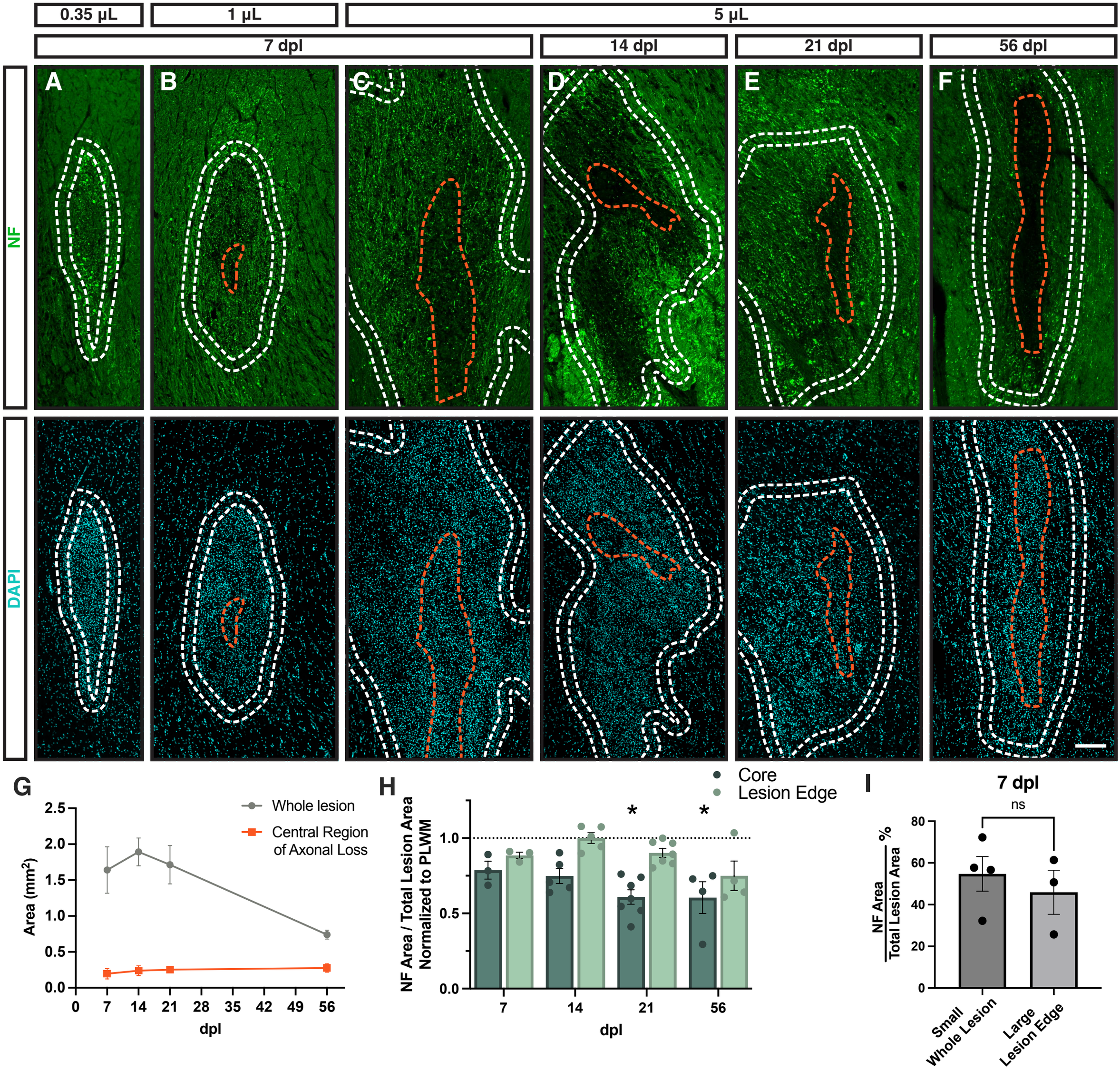
0.35 µL
1 µL
5 µL
7 dpl
14 dpl
21 dpl
56 dpl
A
B
C
D
E
F
NF
DAPI
G
Whole lesion
Central Region of Axonal Loss
Area (mm²)
dpl
H
Core
Lesion Edge
NF Area / Total Lesion Area Normalized to PLWM
dpl
I
7 dpl
ns
NF Area / Total Lesion Area %
Small Whole Lesion
Large Lesion Edge

A

	Rabbit				Mouse	
	Large Lesion		Small Lesion		Spinal Cord	
Parameter	Peak	Values	Peak	Values	Peak	Values
OPC Repopulation	14 dpl	ns	14 dpl	ns	*7 dpl*	↑↑
OL Repopulation	21 dpl	ns	21 dpl	ns	*14 dpl*	↑↑
% Activated OPC ($Sox2^+Olig2^+$)	14 dpl	↑↑	14 dpl	↑	*5 dpl*	↑↑
% Proliferating OPC ($Ki67^+Olig2^+$)	14 dpl	↑	14 dpl	ns	*5 dpl*	↑

B

Large Rabbit Lesions

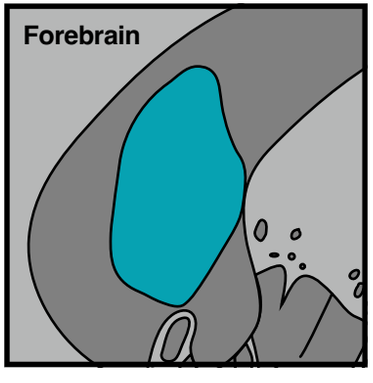

Small Rabbit Lesions

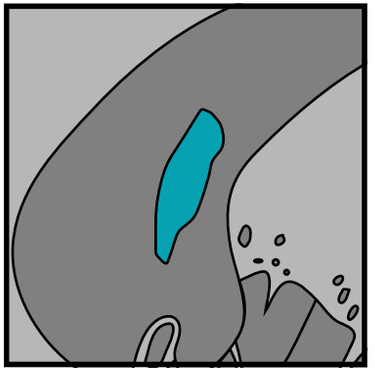

Mouse Spinal Cord
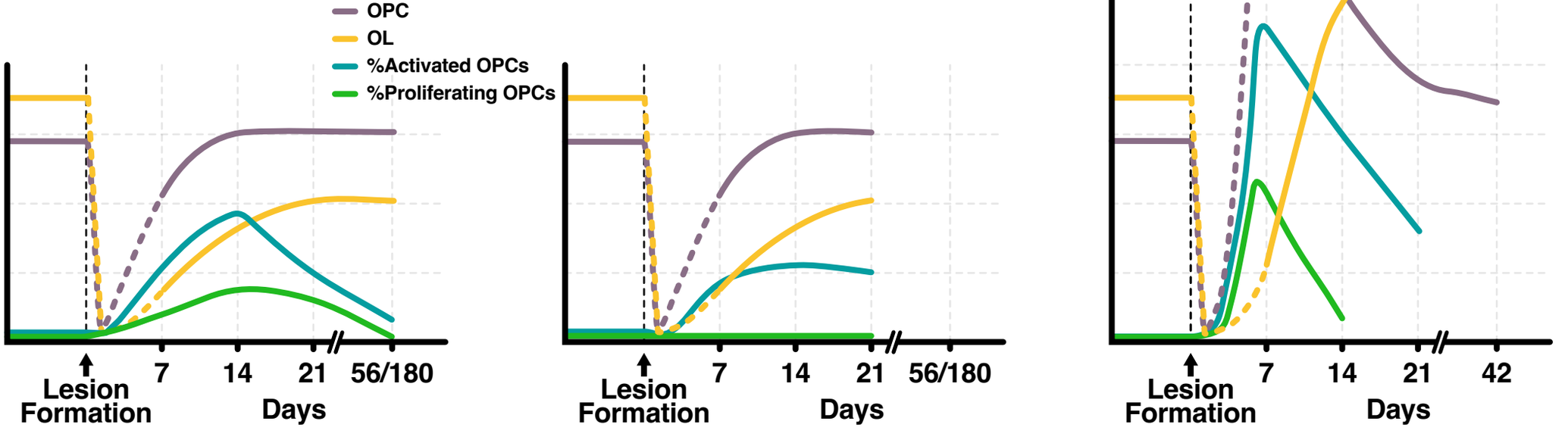
C